

RESEARCH ARTICLE

10.1029/2018JC014838

Characterization of Intraseasonal Kelvin Waves in the Equatorial Pacific Ocean

A. V. Rydbeck¹ , T. G. Jensen¹ , and M. Flatau² ¹U.S. Naval Research Laboratory, Stennis Space Center, Hancock County, MS, USA, ²U.S. Naval Research Laboratory, Monterey, CA, USA

Key Points:

- Methodologies for identifying former and current intraseasonal Kelvin waves using observed sea surface height anomalies are developed
- For Kelvin waves, the dominant processes controlling the upper ocean warming and cooling patterns shift near 150°W
- Kelvin wave kinetic energy is significantly enhanced during El Niño versus La Niña

Correspondence to:

A. V. Rydbeck,
adam.rydbeck@nrlssc.navy.mil

Citation:

Rydbeck, A. V., Jensen, T. G., & Flatau, M. (2019). Characterization of intraseasonal kelvin waves in the equatorial Pacific Ocean. *Journal of Geophysical Research: Oceans*, 124. <https://doi.org/10.1029/2018JC014838>

Received 4 DEC 2018

Accepted 10 MAR 2019

Accepted article online 13 MAR 2019

Abstract Kelvin waves in the equatorial Pacific Ocean are an important subseasonal modulator of upper-ocean thermal and kinetic energies. This study develops a methodology for the objective identification of the waves, including their phase and amplitude, that is based on satellite-derived sea surface height anomalies. Composite analysis of intraseasonal Kelvin waves based on the newly developed index reveals important patterns of wave evolution across the Pacific Ocean. The waves maintain an average phase speed of 2.55 m/s, with maximum of 2.73 m/s when the downwelling portion of the wave is near 150°W and minimum of 2.35 m/s near 175°W. Kelvin waves attain their maximum amplitude at 150°W, the region where intraseasonal surface wind forcing strongly relaxes, and the waves transition from a forced to a freely propagating mode. The dominant processes controlling the mixed-layer temperature also shift near 150°W. Intraseasonal SST anomalies associated with the waves have maximum amplitude of ± 0.25 °C at 140°W, with much stronger anomalies, ± 1.4 °C, along the thermocline at 155°W. Waves strengthen the eastward equatorial undercurrent by 76% while shifting its maximum 3,500 km to the east. The El Niño Southern Oscillation exerts considerable control over the vigor of Kelvin waves, with statistically significant increases of kinetic energy during El Niño versus La Niña periods. For the benefit of the ocean forecasting community, a counterpart intraseasonal Kelvin wave index is developed that avoids the use of forward time filtering such that wave information is available in real time.

Plain Language Summary A new way of identifying and tracking ocean waves that are important to the development of El Niño is created. This new way of identifying the waves is unique because it selects a single type of wave in a sea of many different kinds of waves. These waves, called equatorial Kelvin waves, grow in the west Pacific Ocean and weaken in the east Pacific Ocean. They transport large amounts of heat across the Pacific Ocean and are shown to be strong enough to reverse the direction of the upper ocean currents in certain regions. The ocean tends to warm or cool immediately after the waves have passed and the reasons for this change as the wave moves eastward. The waves are significantly stronger when an El Niño is occurring versus when a La Niña is occurring. During La Niña, Kelvin waves are weak and do not travel across the entire Pacific basin.

1. Background

Kelvin waves (W. Thomson, 1880), initially derived as a solution to a particular case of vanishing meridional velocity within Laplace's dynamical theory of the tides, are a free-wave solution to the perturbation shallow water model equations on an equatorial β plane (Matsuno, 1966). Kelvin waves are nondispersive, and the first-mode baroclinic Kelvin wave accounts for much of the observed eastward intraseasonal wave activity in the equatorial Pacific with a spectral peak near 70 days and a phase speed of ~ 2.7 m/s (Busalacchi et al., 1983; Cravatte, 2003; Enfield et al., 1987; Eriksen et al., 1983; Eriksen & Richman, 1988; Farrar, 2008; Feng et al., 2016; Gasparin et al., 2015; Hayes & Halpern, 1984; Hendon et al., 1998; Kessler et al., 1995; Knox & Halpern, 1982; Kutsuwada & McPhaden, 2002; Lukas et al., 1984; McPhaden, 2002; McPhaden et al., 1988; McPhaden & Taft, 1988; Roundy & Kiladis, 2007; Shinoda et al., 2008, 2009; Thomson & Davis, 2017; Zhang, 2001). The phase speed for Kelvin waves is defined by $c^2 = g'h$, where c is the phase speed, g' is the reduced gravity, and h is the thermocline depth. Using the relationship, $k = \omega / c$ where ω is the frequency and k is the zonal wave number, Kelvin waves with the aforementioned characteristics correspond to zonal wave numbers 2–3. The observed downward phase propagation of intraseasonal Kelvin waves (IKWs) in the Pacific Ocean suggests the presence of higher-order baroclinic modes (e.g., Cravatte, 2003; Farrar, 2008; Kessler & McCreary, 1993; Kutsuwada & McPhaden, 2002; Lukas & Firing, 1984). In the meridional

direction, waves conform to a Gaussian distribution that is symmetric about the equator. The equatorial Rossby radius of deformation governs the poleward decay of wave amplitude, such that the waves are largely confined between 5°S and 5°N (e.g., Cravatte, 2003; Farrar, 2008).

Kelvin waves are typically forced in the west Pacific Ocean by anomalously westerly surface winds that can arise from a variety of atmospheric phenomena (Luther et al., 1983) such as the Madden-Julian Oscillation (MJO), monsoon, extratropical intrusions, and twin cyclones (Seiki & Takayabu, 2007, and references therein). Anomalous westerlies oppose the prevailing easterly trade winds in the equatorial Pacific that are responsible for maintaining the zonal thermocline slope and the deep reservoir of warm water in the west Pacific Ocean. The weakening of the trades relaxes the thermocline slope and redistributes thermal energy from the west Pacific to the east Pacific. Equatorial Kelvin waves are a critical component of this process because, by oceanic equatorial wave standards, they swiftly (2–3 months) transport energy across the basin. The anomalous wind stress modulates mass along the equator such that westerly (easterly) wind stress drives a downwelling (upwelling) Kelvin wave that propagates eastward with anomalous eastward (westward) surface currents. The downwelling Kelvin wave depresses the thermocline by tens of meters which, in turn, increases the ocean heat content (OHC) above the thermocline and raises the sea level elevation by several centimeters (e.g., Kutsuwada & McPhaden, 2002).

Equatorial Kelvin waves modulate the thermal characteristics of the upper ocean, impacting variability in the coupled atmosphere-ocean system across many time scales. Most notably, IKWs contribute to the onset and development of El Niño events (Batstone & Hendon, 2005; Bergman et al., 2001; Boulanger & Menkes, 1995; Harrison & Schopf, 1984; Karnauskas, 2013; Kessler & Kleeman, 2000; Kessler & McPhaden, 1995; Lengaigne et al., 2002, 2003, 2004; Lukas et al., 1984; McPhaden et al., 1992; McPhaden, 1999; McPhaden et al., 1988, 2015; McPhaden & Yu, 1999; Mosquera-Vásquez et al., 2014; Roundy & Kiladis, 2007; Seo & Xue, 2005; Wyrski, 1975, 1977; Zhang, 2001; Zhang & Gottschalck, 2002). While considerable attention has been devoted to the relationship between Kelvin waves and the El Niño Southern Oscillation (ENSO), Kelvin waves are also known to modulate other atmospheric and oceanic phenomena including east Pacific tropical cyclones (Boucharel et al., 2016), eastward propagating atmospheric convective envelopes (e.g., Gribble-Verhagen & Roundy, 2010; Roundy & Gribble-Verhagen, 2010), and tropical instability waves (Giese & Harrison, 1990; Harrison & Giese, 1988; Holmes & Thomas, 2016).

The mechanisms by which Kelvin waves modulate upper ocean temperature vary as waves propagate eastward (e.g., Kessler et al., 1995; McPhaden, 2002; Zhang, 2001). In the central Pacific Ocean, downwelling Kelvin waves advect warm water to the east resulting in locally increased mixed-layer temperatures (Johnson & McPhaden, 1993; Kessler et al., 1995; Kessler & Kleeman, 2000; McPhaden, 2002). This is often supplemented by advection from currents directly forced by westerly wind events (e.g., Lengaigne et al., 2002). In the east Pacific, downwelling Kelvin waves deepen the thermocline, modulating vertical temperature gradients and, as a consequence, vertical advection and entrainment (e.g., Matthews et al., 2007; McPhaden, 2002; Zhang, 2001). A combination of zonal advection with vertical advection and entrainment sometimes results in a zonally elongated region of warm sea surface temperatures (SSTs) along the equator that does not necessarily propagate with the Kelvin wave. In the west Pacific, westerly wind events that generate Kelvin waves are often associated with enhanced atmospheric convection. The winds and convection result in a local cooling effect due to enhanced latent heat fluxes and reduced incoming shortwave radiation at the ocean's surface. The intraseasonal cooling in the west Pacific by atmospheric convection and warming by Kelvin waves in the central and eastern Pacific may then rectify onto interannual time scales via a positive Bjerknes (1969) feedback.

Kelvin waves behave differently under varying atmospheric and oceanic conditions, particularly as they relate to ENSO (Benestad et al., 2002; Busalacchi & Cane, 1988; Dewitte et al., 2008; Giese & Harrison, 1990; Harrison & Schopf, 1984; Kindle & Phoebus, 1995; Long & Chang, 1990; Mosquera-Vásquez et al., 2014; Puy et al., 2016; Roundy & Kiladis, 2006; Schopf & Harrison, 1983; Shinoda et al., 2008), making the waves a subordinate as well as a stimulus of interannual variability. Benestad et al. (2002) used an ocean general circulation model with varying ENSO phases but identical intraseasonal forcing to demonstrate that the Kelvin wave phase speed is greater during El Niño versus La Niña periods owing to a deeper thermocline. The wave amplitudes were also greater during El Niño. La Niña conditions were characterized by increased vertical shear in the upper ocean which strongly attenuated the wave energy such that the waves atrophied

and did not reach the eastern coast. However, Roundy and Kiladis (2006) observed that Kelvin wave phase speeds systematically decreased during El Niño onset, opposite to that expected for a deepening thermocline. Building on the work of Roundy and Kiladis (2006), Shinoda et al. (2008) used an ocean general circulation model to show that intraseasonal wind forcing in the central and east Pacific drove the observed Kelvin wave phase speed variability. This effect might easily be overlooked because the central and eastern Pacific wind forcing is much weaker than the forcing that generated Kelvin waves in the west Pacific. Little sensitivity was shown to variations in the background oceanic state during these experiments, emphasizing the role of the atmospheric forcing for varying Kelvin wave phase and amplitude during different ENSO background states. This result suggests that oceanic mechanisms associated with thermocline variability, viscous dissipation, energy transfer among Kelvin wave vertical modes, Doppler shifting by equatorial undercurrents, and nonlinear advection play a secondary role. We contribute to the ongoing discussion regarding Kelvin wave sensitivity to various ENSO phases by systematically examining their variability using a suite of data products.

The purpose of this study is to develop a methodology for the objective identification of IKWs in order to investigate their salient characteristics. Utilizing these methods, composites of Kelvin waves are constructed using satellite-based data fields and a 22-year ocean reanalysis product in order to study details of their genesis, propagation, termination, upper ocean effects, and ENSO-related interannual variability. A counterpart Kelvin wave index available in real time is also created to assist the monitoring by operational forecast centers of subseasonal heat and momentum transports across the Pacific Ocean. Section 2 describes the Hybrid Coordinate Ocean Model (HYCOM) reanalysis product and observational data used to analyze Kelvin wave features. Section 3 describes the development of an objective framework for identifying an IKW's phase and amplitude that is then used to formulate wave composites. Section 4 examines the composites of Kelvin wave surface fields as well as temperature and zonal velocity in the upper 350 m of the ocean. A simplified IKW mixed-layer temperature budget is also analyzed. In section 5, the sensitivity of Kelvin wave propagation, maintenance, and amplitude to the state of ENSO, previously shown to modulate the wave's phase speed and amplitude (i.e., Roundy & Kiladis, 2006), are evaluated. Conclusions are presented in section 6.

2. Data

2.1. HYCOM Reanalysis

The HYCOM (www.hycom.org) is a general ocean circulation model currently used as the ocean component of the U.S. Navy's global ocean forecast system (Metzger et al., 2014; Yu et al., 2015, 2017). HYCOM is a primitive equation model that is integrated forward in time using a split-explicit treatment of barotropic and baroclinic modes. The hybrid coordinate refers to the mix of model vertical coordinate systems. HYCOM utilizes a combination of fixed z , terrain-following sigma, and isopycnal coordinates to ensure sufficient resolution for resolving mixed-layer processes, shallow coastal regions, and stratified regions (Chassignet et al., 2003). Particulars of HYCOM are presented in Bleck (2002) with model details relevant to the present study briefly described below.

HYCOM has 41 layers in the vertical with a horizontal grid spacing of 0.08° (~ 9 km at the equator). The top 14 layers of HYCOM are fixed in sigma- z level space and confined to the upper 84 m, resulting in improved representation of mixed-layer processes, an advancement over the previous version of HYCOM with 32 vertical levels (Metzger et al., 2017). Other recent enhancements to the model are the inclusion of surface currents when calculating the atmospheric wind stress (Yu et al., 2017), upgrades to wind stress and heat flux coefficients by using variable atmospheric surface pressure (vs. constant surface pressure), and improvements to ocean turbidity representation owing to the development and use of monthly chlorophyll climatologies (Jolliff & Smith, 2014). The latest HYCOM reanalysis comprises the years 1994–2015 and uses surface forcing fields from the National Centers for Environmental Prediction Climate Forecast System Reanalysis (Saha et al., 2010) during the same period.

The HYCOM reanalysis also employs the Navy COupled Data Assimilation (NCODA) system (Cummings, 2006). NCODA is a fully 3-dimensional, multivariate, variational ocean data assimilation scheme that integrates fields such as sea surface height (SSH), SST, sea ice concentration, temperature, and salinity from

altimeters, in situ observations such as ships, buoys, expendable bathythermographs, CTDs, and Argo floats among others. A more complete list of observational data types ingested into NCODA is available in Cummings and Smedstad (2013), but new sources are frequently added. The Improved Synthetic Ocean Profile (ISOP) system in NCODA also generates synthetic temperature and salinity profiles that are based on historical observations of the ocean's surface and subsurface (Helber et al., 2013; Townsend et al., 2015). ISOP replaced the modular ocean data analysis system (Fox et al., 2002) used in previous versions of NCODA. The ISOP system employs a more versatile 1-D variational approach to utilize historical vertical covariances that preserve the relationships between surface and subsurface ocean variables as well as the vertical gradients of the subsurface variables, resulting in an overall improvement of the ocean's vertical structure in the reanalysis.

2.2. Observations

SSH anomalies are used to identify the leading patterns of IKW variability. The SSH anomalies are obtained from the Archiving, Validation, and Interpretation of Satellite Oceanographic (AVISO) data set (0.25°; Pascual et al., 2006) covering the years 1993–2016. Gridded and near real-time SSH anomaly fields from AVISO are interpolated in space and time with a repeated satellite track approximately occurring every 10 days and, because of this latency, may not meet the demands of certain operational forecast centers. In those cases, assimilative SSH analyses from global ocean models, such as HYCOM, that are available at more frequent time intervals may serve as a suitable alternative.

Observational data used for compositing included surface currents, SST, zonal pseudostress, and the previously discussed SSH. Surface currents from the Ocean Surface Current Analysis Real-time (OSCAR; 1/3°; Bonjean & Lagerloef, 2002; ESR, 2009) project from 1993–2016 are used. OSCAR surface currents are linearly interpolated from pentad to daily data for use in compositing with other daily fields. SSTs from the National Oceanic and Atmospheric Administration (NOAA) daily optimum interpolation V2 (0.25°) that includes a combination of Advanced Very High Resolution Radiometer (AVHRR) and Advanced Microwave Scanning Radiometer-Earth observing system are utilized (Reynolds et al., 2007). The Advanced Microwave Scanning Radiometer-Earth/AVHRR data are used for June 2002 to October 2011, and the AVHRR-only data are used for the remainder of the 1993–2016 period. The zonal pseudostress ($u|u|$) is calculated using 0.75° × 0.75° European Centre for Medium-Range Weather Forecasts Interim Reanalysis (Dee et al., 2011) 10-m zonal winds.

3. IKW Identification Methods

In order to analyze features of IKWs that are representative of typical waves in the Pacific Ocean, a methodology is developed to objectively determine phase and amplitude information for use in Kelvin wave composite analyses. The methods for classifying Kelvin waves are analogous to methods utilized for atmospheric intraseasonal variability, specifically that of the MJO (Kiladis et al., 2014; Liu et al., 2016; Ventrice et al., 2013; Wheeler & Hendon, 2004) and the boreal summer intraseasonal oscillation (BSISO; Kikuchi et al., 2012; Lee et al., 2013). We perform a single variable empirical orthogonal function (EOF) analysis but first preprocess the data with an intraseasonal frequency and eastward wave number filter to isolate variability associated with IKWs. We also develop a counterpart methodology that is available in real time. Details of the respective methodologies are described below.

3.1. IKW Index

The IKW index is based on SSH anomalies that are first prepared by removing the first three harmonics of the seasonal cycle. The SSH anomalies are then filtered in wave number space such that wave numbers greater than or equal to 0, that is, eastward wave numbers, are retained. SSH anomalies are also band-pass filtered using a 20–180-day Lanczos filter in order to broadly isolate intraseasonal variability. Next, EOFs are calculated using SSH anomalies in the region from 2°S to 2°N and 150°E to 90°W. The narrow latitude band is selected to isolate the main region of IKW variability and to minimize any potential contamination by Rossby waves that may be eastward propagating due to Doppler shifts by the background currents. The leading EOFs describe 35.5% and 34.7% of the SSH variability. In order to show the patterns of the leading EOFs, unfiltered SSH anomalies are linearly regressed onto the corresponding principal components (PCs) of EOFs 1 and 2 (Figure 1). The first and second EOFs are characterized by maxima/minima centered on the equator

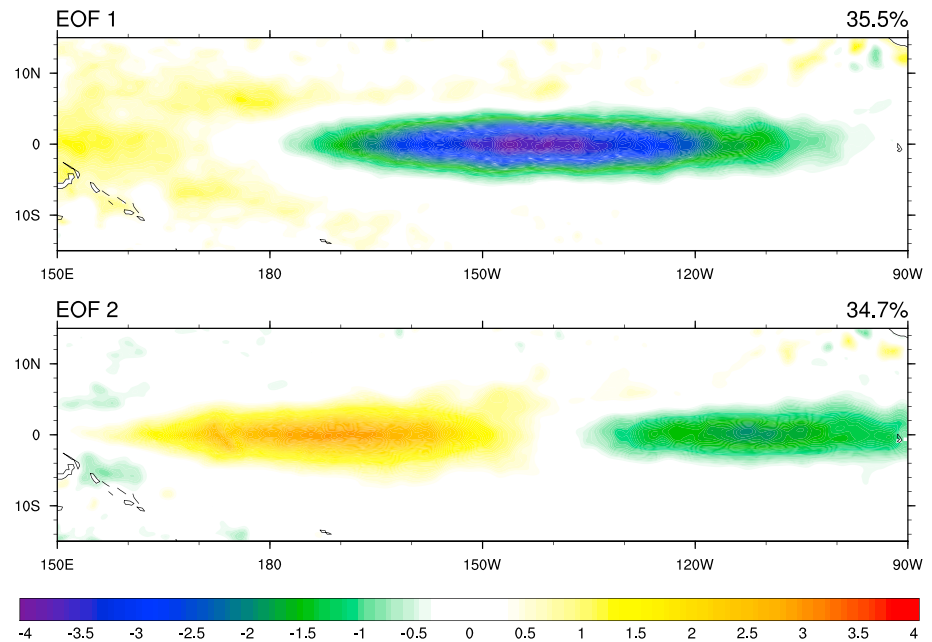


Figure 1. Linear regressions of unfiltered sea surface height (cm) anomalies onto the respective principal components of the two leading EOFs are shown with percent variance explained by each EOF in the upper right above each panel. EOF = empirical orthogonal function.

with a Gaussian distribution in latitude. The SSH patterns are largely confined within 5° of the equator and correspond to zonal wavelengths of $\sim 13,000$ – $20,000$ km. The first two EOFs are distinguishable from the lower modes according to the criterion of North et al. (1982; Figure 2a), indicating that the distinctiveness of the first two EOFs are not due to sampling errors. The corresponding PCs of EOFs 1 and 2 are phase lagged with a correlation of 0.85 when PC1 leads PC2 by 14 days (Figure 2b). The power spectra for PC1 and PC2 are also shown in Figures 2c and 2d, with statistically significant peaks near 70 and 50 days, consistent with previously observed broadband IKW power.

Information contained in the leading pairs of EOFs and PCs are employed to derive IKW phase and amplitude information. Similar methods are routinely used for the MJO and BSISO previously mentioned. After normalizing PC1 and PC2 to have a standard deviation of 1, the IKW's amplitude and phase are calculated using the following formulas:

$$\text{Amplitude} = \sqrt{(\text{PC1}^2 + \text{PC2}^2)}, \quad (1)$$

$$\text{Phase} = \tan^{-1}\left(\frac{\text{PC2}}{\text{PC1}}\right). \quad (2)$$

As in previous studies of atmospheric intraseasonal variability (e.g., Wheeler & Hendon, 2004), the phase angles range from 0° to 360° and are subdivided into eight equal phases of 45° length such that each phase represents 6–9 days of the IKW life cycle. Phase and amplitude information can then be used to construct phase composites of robust IKWs in order to identify consistent patterns among diverse IKW events (see Figures 8 and 9). The IKW index amplitude is shown in Figure 3 with red shading indicating El Niño events and blue shading for La Niña events. Unless otherwise noted, IKWs are composited for periods when the IKW index is greater than 1.5 (black line in Figure 3). Kelvin waves identified by the IKW index can be reconstructed for a particular time, t , by the following formula:

$$\text{SSH}_{\text{Kelvin Waves}}(t) = \text{EOF1} \times \text{PC1}(t) + \text{EOF2} \times \text{PC2}(t). \quad (3)$$

To ensure that the IKW index appropriately represents the eastward propagation of intraseasonal SSH anomalies associated with IKWs, an additional lag correlation analysis is performed as in Wang et al. (2018). The lag correlation is referenced to SSH anomalies averaged from 2°S – 2°N and 160 – 150°W that

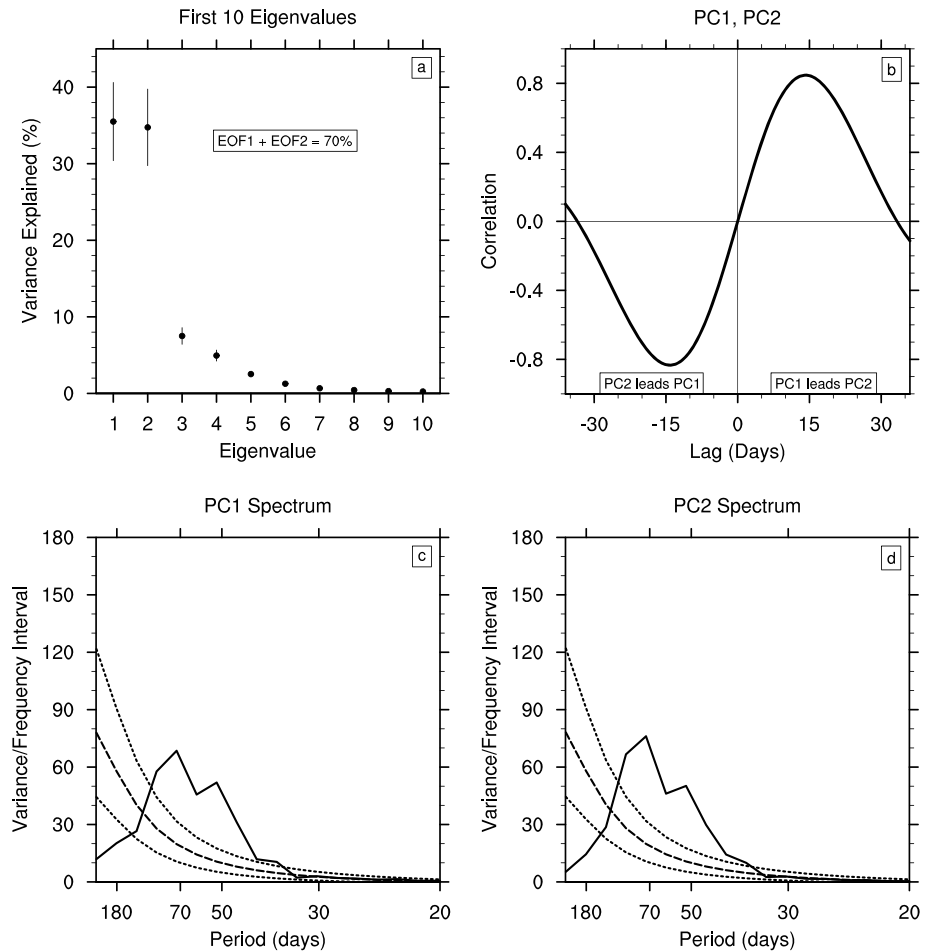


Figure 2. The (a) variance explained by the first 10 EOFs (dots) with standard errors (lines), (b) lag correlation of the first two PCs, (c) power spectrum of PC1, and (d) power spectrum of PC2 are shown. The power spectra (c and d) are shown with the 99% and 1% upper and lower significance levels (dotted lines) and the red noise spectrum (dashed lines). PC = principal component; EOF = empirical orthogonal function.

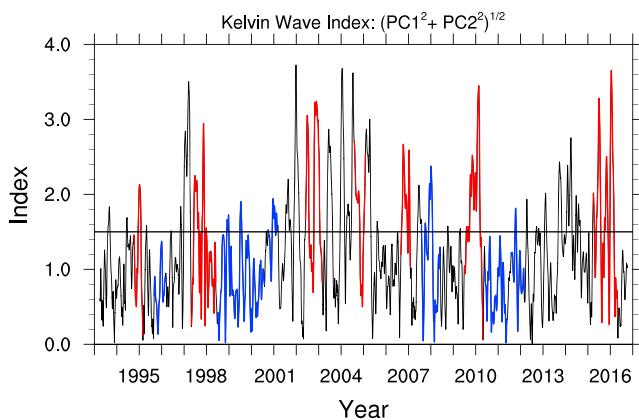


Figure 3. The amplitude of the Kelvin wave index from 1993–2016 is shown. Red shading indicates El Niño events, and blue shading indicates La Niña events. El Niño (La Niña) events are defined as those in which the 3-month running mean SST in the Niño 3.4 region is greater (less) than +0.5 °C (−0.5 °C) for at least 5 months. The 1.5 threshold for the intraseasonal Kelvin wave index that is used for compositing is shown in black. PC = principal component.

are filtered to retain eastward propagating (wave numbers ≥ 0) and intraseasonal (30–120-day band-pass) filtered variability. In Figure 4a, the lag correlation of the reference SSH with the IKW SSH anomalies calculated using equation (3) is shown. The resulting correlation pattern shows a signal that coherently propagates eastward at a phase speed consistent with Kelvin waves (e.g., Cravatte, 2003), indicated by the black line. A similar lag correlation is performed using the reference SSH correlated with wave number and intraseasonal-filtered SSH anomalies averaged from 2°S–2°N at all longitudes (Figure 4b). This is representative of the observed propagation characteristics of IKWs. The observed lag correlation pattern (Figure 4b) is similar to that using the IKW index (Figure 4a) with comparable lag correlation values as well as phase speeds, indicating that the IKW index represents realistic eastward propagation of IKWs.

An example of the IKW index's utility is presented in Figure 5. Figure 5a shows the total AVISO SSH anomalies (shading) and the reconstructed Kelvin wave (contours). The total SSH anomalies are unsuitable for delineating Kelvin wave features during this period. When the reconstructed Kelvin wave is compared with SSH anomalies filtered to retain

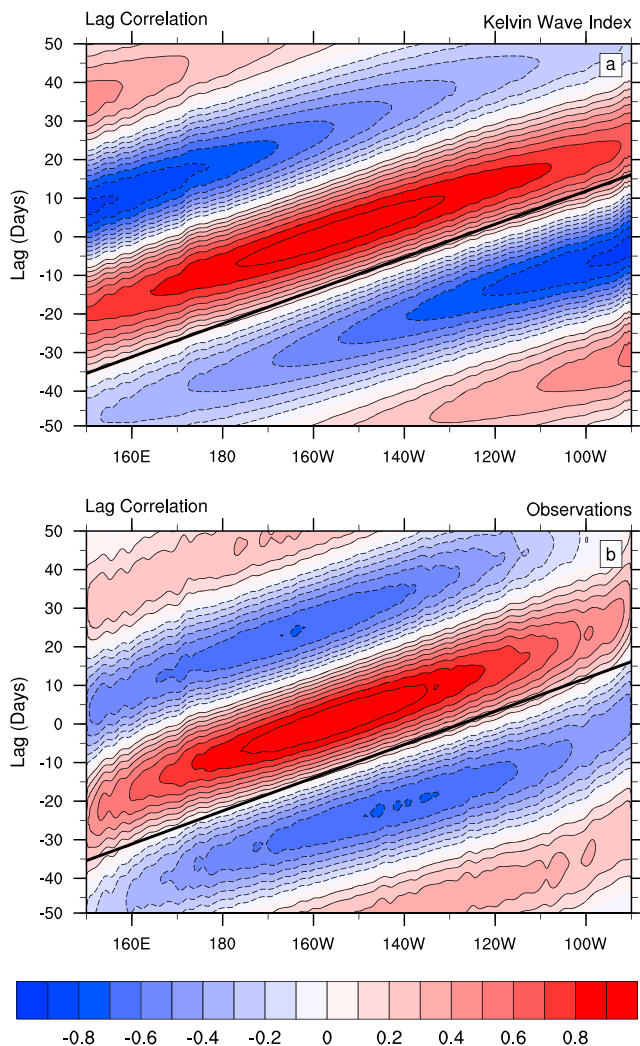


Figure 4. Eastward wave number and 30–120-day band-pass-filtered SSH anomalies averaged from 2°S–2°N and 160–150°W are lag correlated with (a) SSH anomalies derived from the Kelvin wave index using equation (3) and (b) eastward wave number and 30–120-day band-pass-filtered SSH anomalies averaged from 2°S–2°N. The correlation contour interval is 0.1 with the zero contour omitted. The black line indicates a phase speed of 2.9 m/s. SSH = sea surface height.

intraseasonal and eastward propagating variability (Figure 5b), SSH anomalies derived from the IKW index largely agree with the position, timing, and amplitude of upwelling and downwelling IKWs. For example, robust downwelling and upwelling waves in the central Pacific Ocean from January–April 1997 that were critical for the development of the 1997–1998 El Niño event (McPhaden, 1999) are captured by the IKW index. There are intermittent deficiencies of the index, such as the overestimation of downwelling wave activity in the western and central Pacific in November 1997. A limitation of the index arises when IKWs are weak and/or short-lived as observed in April–May 1997 in the western Pacific Ocean.

An additional use of the index is the derivation of average Kelvin wave phase speeds and their geographical variation. Figure 6 shows the 30–120-day band-pass-filtered SSH anomalies averaged from 2°S–2°N and composited for the eight phases of the IKW index. The entire cycle of Kelvin wave propagation takes ~70 days to complete, such that each phase represents 8.75 days of the IKW life cycle. The phase speeds are derived by correlating in longitude the magnitudes of SSH anomalies with the phases before and after the phase of interest. For example, to determine the phase speed for phase 4, the SSH magnitudes for phases 3 and 5 are correlated in longitude. The longitude at which the correlation maximizes determines the distance traveled which is then used to calculate a phase speed, similar to the methods of Mosquera-Vásquez et al. (2014). The average phase speed of the IKW over all phases is 2.55 m/s and remains relatively unchanged regardless of the precise IKW index threshold used. This generally agrees with theoretical phase speeds for the first baroclinic mode Kelvin wave in the equatorial Pacific (e.g., Chelton et al., 1998). Discrepancies between the observed and theoretical phase speeds may result from wind stress, mean currents, discrepancies in the thermocline depth, and influence of higher-order baroclinic modes. The IKWs accelerate from phase 2 to phase 4, from 2.35–2.73 m/s. The IKWs decelerate after phase 4, eventually decelerating to 2.44 m/s by phase 8.

Finally, we briefly analyze the phases during which downwelling IKWs initiate. For these purposes, initiation is defined as the time at which the IKW index exceeds 1.0 standard deviation and proceeds for at least 270° of the phase space while maintaining an amplitude of at least 1.0. Of the 89 KWs with amplitudes greater than 1.0, 29 of those are maintained for at least 270°, with 14 (48%) initiating during phase 8, 13 (45%) during phase 7, and 2 (7%) during phase 1. IKW initiation exhibits impor-

tant sensitivities to the prescription of the duration and amplitude criteria. For example, the number of qualifying IKWs is 36 when the amplitude threshold is increased to 1.5 and the continual phase propagation is reduced to 135° with 11 (31%) initiating during phase 8, 6 (17%) during phase 2, 5 (14%) during phase 7, 5 (14%) during phase 1, 3 (8%) during phase 6, and 2 (5%) during phases 5, 4, and 3.

3.2. Real-Time IKW Index

A shortcoming of the band-pass-filtered IKW index is that it requires forward temporal filtering and is thus not available in real time. A common practice to overcome this limitation is to project SSH anomalies that are available in real time onto the leading EOFs of the IKW index. The resulting PCs are used to derive IKW phase and amplitude information in real time (e.g., Kikuchi et al., 2012; Kiladis et al., 2014). The following steps are taken to obtain a real-time IKW index that approximates the IKW index.

The first three harmonics of the seasonal cycle are subtracted from the SSH anomalies and then filtered to isolate eastward wave numbers greater than or equal to 1. To remove low-frequency variability from the SSH anomalies, we calculate the mean of the 55 days previous to the time of interest and subtract that

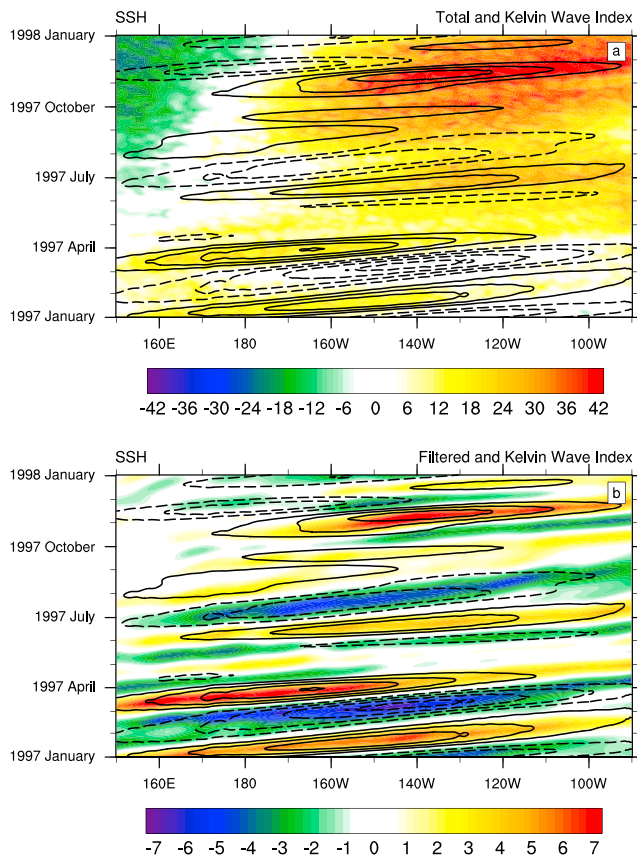


Figure 5. SSH anomalies (cm) averaged from 2°S–2°N for the year 1997 are shown. The shading in (a) shows the unfiltered SSH anomalies. The shading in (b) shows the eastward wave number and 30–120-day band-pass-filtered SSH anomalies. The contour lines are the same in both panels and show the reconstructed Kelvin wave SSH anomalies using equation (3). Contour line spacing is 2 cm and omits the zero contour line. Positive SSH anomalies are solid, and negative anomalies are dashed. SSH = sea surface height.

mean from the data. The SSH anomalies are then projected onto the EOFs of the IKW index. The parameters of the wave number filter and prior running mean are selected such that the correlation of the real time PCs with the PCs from section 3.1 are optimized for the entire 1993–2016 period. The bivariate correlation between PC1 of the IKW index and PC1 of the real time IKW index is 0.87 when the real-time PC1 leads by 1 day. For PC2, the correlation is 0.86 when the real-time PC2 leads by 2 days. The strong correlation between the respective PCs indicates that the real-time IKW index may serve as a suitable proxy of the IKW index when contemporary information is necessary. Time series of PC1 and PC2 for both the IKW index and the real-time IKW index from January to September 1997 are shown in Figure 7. The real-time PCs correspond well with the band-pass-filtered PCs over much of the period. Similar methods used to analyze the MJO and BSISO have utilized tapered running averages to dampen high-frequency variability. In initial testing, such smoothing did not improve the correlations of the PCs derived from AVISO SSH data but might be advantageous when using noisier inputs.

4. IKW Composites

4.1. General Features

Composites of IKWs are shown in order to characterize their archetypal behavior and are based on periods when the IKW index is greater than 1.5. Figure 8 shows composites of 30–120-day band-pass-filtered AVISO SSH and OSCAR surface current anomalies. The number of days averaged to formulate each phase composite is shown in the upper left of each panel in Figure 8. The downwelling component of the Kelvin wave (positive SSHs) originates in the west Pacific Ocean during phase 8. The IKW propagates eastward while intensifying through phase 4, at which time the downwelling wave maximum is near 150°W. During this strengthening period, currents are convergent along the wave's leading edge and within the wave as expected for a forced downwelling Kelvin wave. The wave gradually weakens as it propagates to the east during subsequent phases.

Upon encountering the eastern boundary during phases 7 and 8, coastal Kelvin waves are observed to propagate poleward. The upwelling portion of the IKW (negative SSHs) exhibits similar behavior to the downwelling wave though of opposite signed SSH and zonal current anomalies.

The composite intraseasonal NOAA SST anomalies (shading) associated with IKWs are shown in Figure 9 along with AVISO SSH anomalies (contours). As the nascent downwelling wave intensifies in the west Pacific Ocean during phases 8 and 1, weakly cool SST anomalies are in phase with the wave, a likely result of cooling effects by enhanced westerly winds (see Figure 11) and atmospheric convection. Warm anomalies develop and strengthen during phases 2–6 and are located 1/8–1/4 wavelength behind the SSH maximum. In phase 6, warm SST anomalies maximize near 140°W with magnitudes of 0.25 °C. This is near the region of greatest SST gradient magnitude (see Figure 13), suggesting that horizontal advection by the eastward currents acting on the mean zonal temperature gradient is likely responsible for the SST anomaly here, as observed in other studies (e.g., McPhaden, 2002). This is further examined in the mixed-layer temperature budget in section 4.3. After phase 6, warm SST anomalies gradually weaken while generally becoming more phase lagged with the downwelling Kelvin wave. The SST pattern is more complicated in the equatorial east Pacific during phase 8, where warm anomalies from 120–90°W rapidly transition to cool anomalies along the coast near 85°W. Similar phasing and amplitudes are observed for the upwelling Kelvin waves, with cool SST anomalies lagging 1/8–1/4 wavelength behind SSH minima during strengthening phases.

The phase lagging of SST anomalies as Kelvin waves enter the east Pacific likely results from the transition from a horizontal advection dominated SST tendency in the west and central Pacific Ocean to a tendency driven by vertical advection and mixing processes associated with thermocline shoaling in the east Pacific

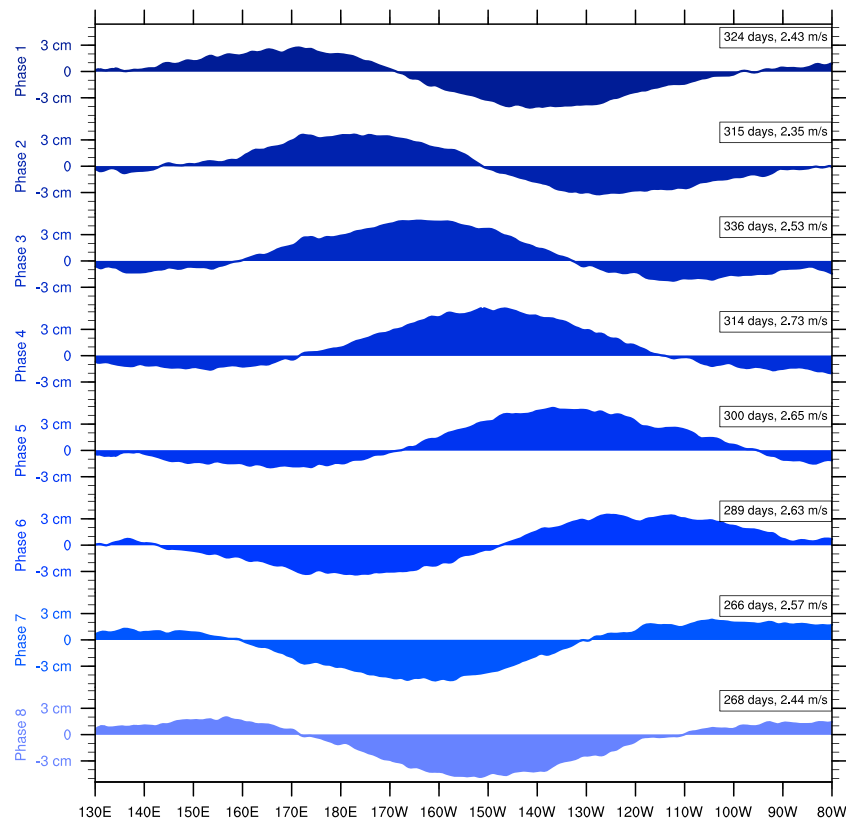


Figure 6. Composites of 30–120-day band-pass-filtered sea surface height anomalies averaged from 2°S–2°N are shown for phases 1–8 of the Kelvin wave index. Each phase represents 8 days of the Kelvin wave life cycle. Kelvin wave phase speeds are shown in the upper right of each panel, with the number of days included in each composite. Distances used for computing the phase speeds are determined by correlating the magnitude of the sea surface height profiles in longitude, finding the maximum correlation for phases before and after the phase of interest, and subtracting the respective longitudes where maximum correlation occurs.

(i.e., Kessler et al., 1995; McPhaden, 2002; Zhang, 2001). Increasing and decreasing the IKW index threshold used for compositing produces corresponding increases and decreases of IKW SSH and SST anomaly amplitude (not shown), while the phasing remains largely unchanged. This suggests that the SST phasing does not strictly depend on Kelvin wave amplitude, but the degree of warming and cooling does. The vertical structure of the anomalous temperature anomalies are examined later in section 4.2 to better analyze the role of thermocline shoaling on temperature variability.

The intraseasonal OHC anomaly from HYCOM reanalysis temperature data is calculated using the following equation:

$$OHC(t, x, y)' = \left(\rho c_p \int_{\text{surface}}^{700\text{m}} T(t, x, y, z) \partial z \right)', \quad (4)$$

where T is the temperature, ρ is the density of sea water (1,027 kg/m³), and c_p is the specific heat of sea water (3,986 J/kg). The composite of intraseasonal OHC anomalies is shown in Figure 10 and displays a systematic phase propagation of OHC and SSH anomalies, unlike SST anomalies. Because the composite is performed for the years with which HYCOM reanalysis is available, the sampling size is reduced by ~4%. Changes owing to the reduced sample size are minor and can be seen by comparing SSH contours for Figures 9 and 10. The OHC and SSH anomaly maxima and minima are phase aligned, propagating across the Pacific Ocean

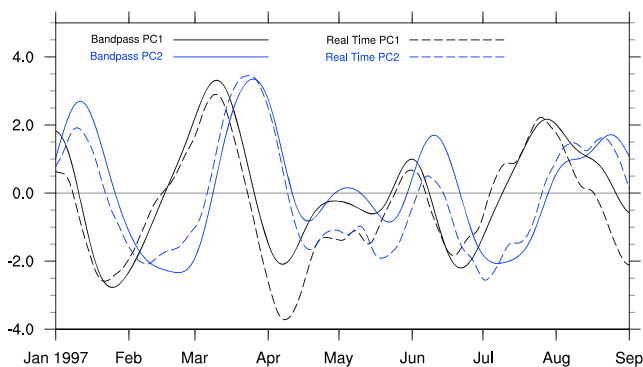


Figure 7. PC1 (black) and PC2 (blue) for the band-pass-filtered intraseasonal Kelvin wave (solid) and real-time intraseasonal Kelvin wave index (dashed) are shown for the period January 1997 to August 1997. PC = principal component.

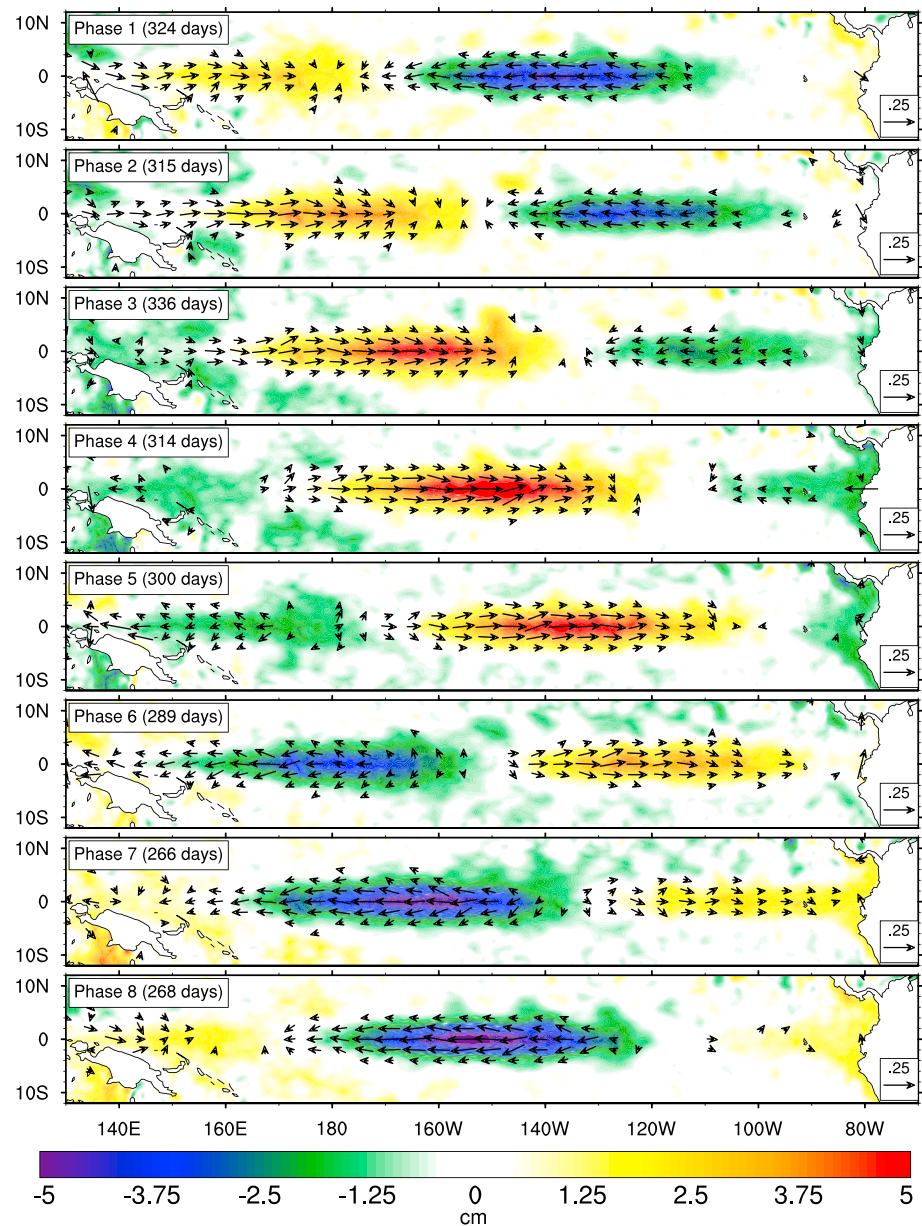


Figure 8. Composites of 30–120-day band-pass-filtered sea surface height (shading, cm) and Ocean Surface Current Analysis Real-time surface currents (vector, m/s) anomalies based on the intraseasonal Kelvin wave index are shown for phases 1–8. The number of days in each composite is shown in the upper left, and the reference current vector is shown in the bottom right of each panel.

with the same phase speeds. This behavior is expected as the same variable modulating the intraseasonal sea surface elevation is also responsible for variations in OHC; this is the thermocline depth along which Kelvin waves propagate and also modulate. For example, a depressed thermocline increases the warm water volume in the ocean above which, in turn, raises the sea level elevation. This same reasoning is used by oceanic forecast centers, such as the NOAA Climate Prediction Center (<http://www.cpc.ncep.noaa.gov/products/GODAS/>), that monitor the 20 °C isotherm, among other analysis products, as a proxy to analyze Kelvin wave phase and propagation. The OHC anomalies maximize in phase 4, when the SSH anomalies likewise maximize. This is two phases earlier than the anomalous SST maximum and is further evidence that SST anomalies are not rigorously regulated by thermocline variations in this region.

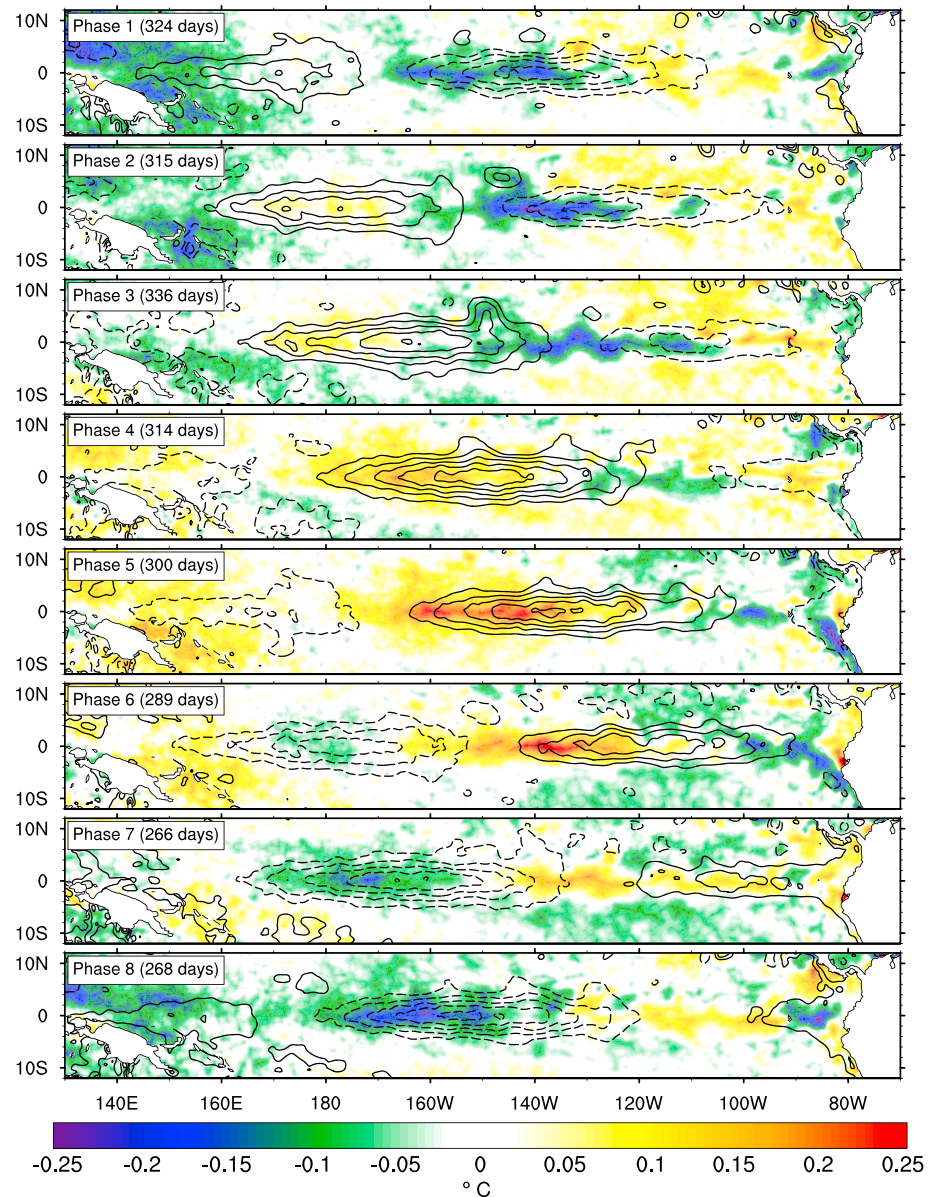


Figure 9. Composites of 30–120-day band-pass-filtered sea surface height (line contours, cm) and National Oceanic and Atmospheric Administration sea surface temperature (shading, °C) anomalies based on the Kelvin wave index are shown for phases 1–8. The number of days in each composite is shown in the upper left. The sea surface height contour interval is 1 cm with the zero contour line omitted. Positive (negative) contours are solid (dashed).

The forcing of Kelvin waves is examined next (Figure 11). The 30–120-day band-pass-filtered zonal pseudostress anomalies ($\langle u|u \rangle$) force downwelling Kelvin waves beginning in phase 7, slightly north of the equator in the west Pacific. The pseudostress maximum extends to the southeast and south of the equator during phases 8 and 1, as Kelvin wave SSH anomalies develop in response to the atmospheric forcing. The positive pseudostress weakens in phases 2 and 3 and is almost entirely diminished by phase 4. The slow eastward-propagating pattern of the pseudostress may be an artifact of compositing many different IKW events that initiate at various phases and during various seasons across the west and central Pacific Ocean. By phase 5, the downwelling wave is freely propagating and reaches maximum SSH amplitude with only weak zonal pseudostress, which is an order of magnitude weaker than the peak pseudostress, along its path to the eastern boundary in subsequent phases. The wavelength of the zonal pseudostress during phases 8, 1, and 2 closely resembles that of the fully developed Kelvin wave, suggesting a role for wave number matching between

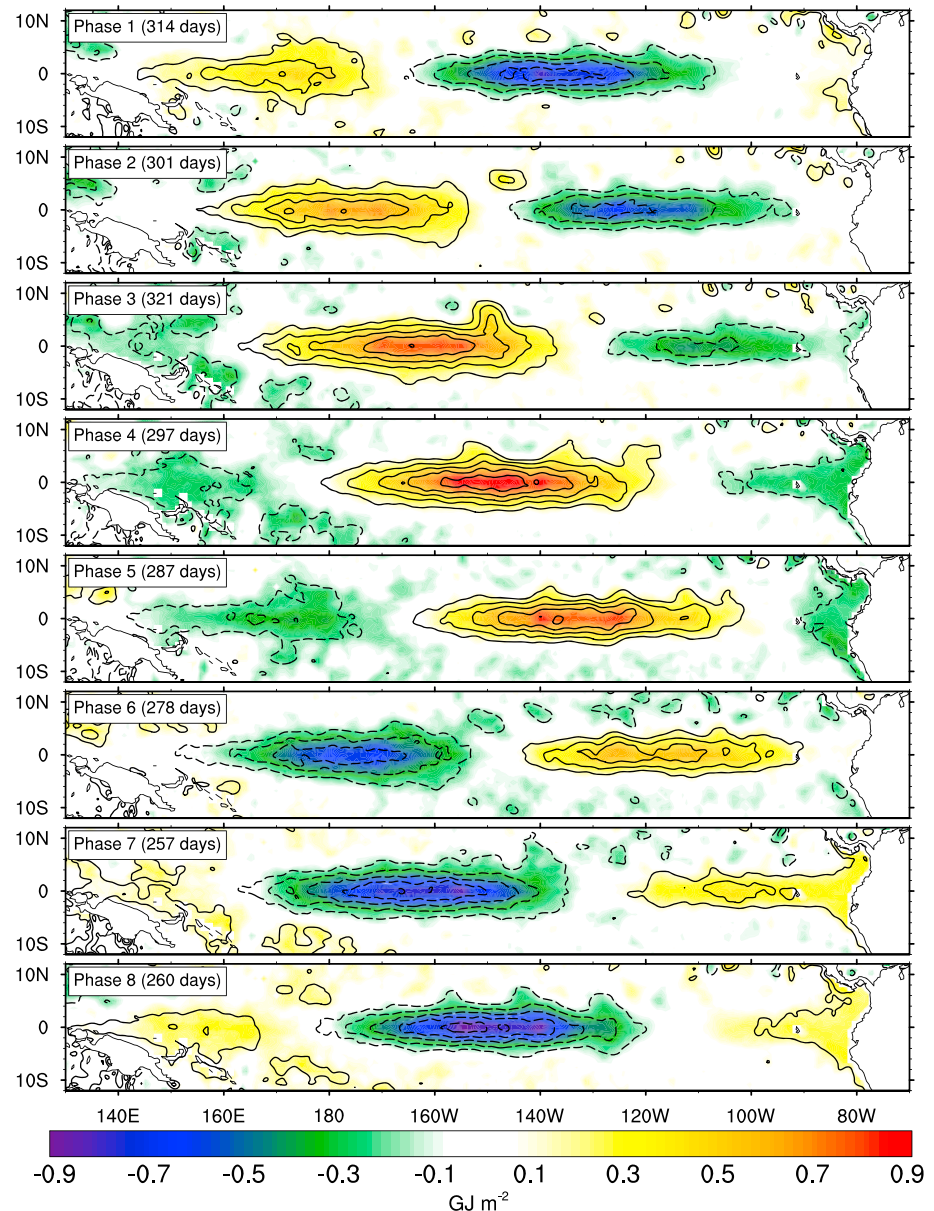


Figure 10. Composites of 30–120-day band-pass-filtered sea surface height (line contours, cm) and 0–700-m ocean heat content (shading, GJ/m^2) anomalies based on the Kelvin wave index are shown for phases 1–8. Ocean heat content values are derived from Hybrid Coordinate Ocean Model reanalysis fields. The number of days in each composite is shown in the upper left. The sea surface height contour interval is 1 cm with the zero contour line omitted. Positive (negative) contours are solid (dashed).

atmospheric forcing and oceanic response. During wave initiation in the west Pacific, the *total* surface winds are weakly westerly to the west of 170°E along the equator (figure not shown). To the east of 170°E , the westerly anomalies are not strong enough to change the sign of the total winds but instead result in a strong relaxation of the prevailing easterlies.

4.2. Vertical Cross Sections

While many features of IKWs are observable from the surface, such analysis only details part of the wave. IKW behavior at and above the thermocline supplements insights derived from surface observations and paints a fuller picture of wave initiation, propagation, and impacts. Previous studies have utilized in situ observations to analyze the vertical profile and longitudinal variation of IKWs in the Pacific (e.g.,

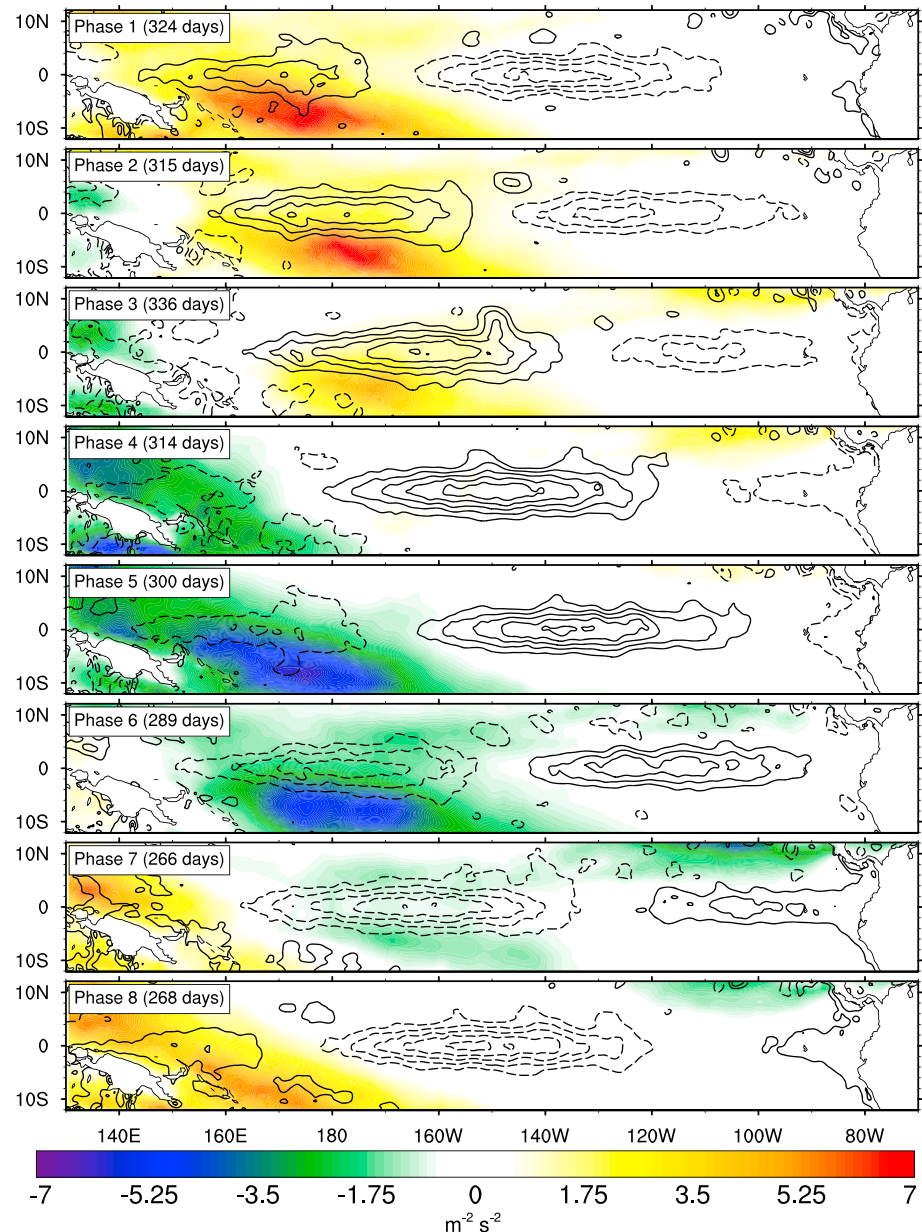


Figure 11. Composites of 30–120-day band-pass-filtered sea surface height (line contours, cm) and European Centre for Medium-Range Weather Forecasts Interim Reanalysis zonal pseudostress (shading, $\text{m}^{-2} \text{s}^{-2}$) anomalies based on the Kelvin wave index are shown for phases 1–8. The number of days in each composite is shown in the upper left. The sea surface height contour interval is 1 cm with the zero contour line omitted. Positive (negative) contours are solid (dashed).

McPhaden, 2002). In an attempt to close the spatial and temporal gaps left unresolved by in situ observations and further build upon previous work, vertical cross section of IKWs are examined using daily HYCOM reanalysis fields described in section 2.1.

The total (shading) and intraseasonal (contours) zonal currents from the surface to 350 m are shown in Figure 12. Kelvin waves are associated with intraseasonal current anomalies that gradually descend and intensify from the west to central Pacific and ascend and weaken in the east Pacific. For example +10-cm/s current anomalies descend from 50 m near 140°E in phase 8 to 200 m near 130°W in phase 4. The +10-cm/s anomalies then ascend to 125 m near 110°W in phase 6. The vertical phase propagation of Kelvin waves has previously been attributed to the interactions of multiple vertical modes (e.g., Kessler &

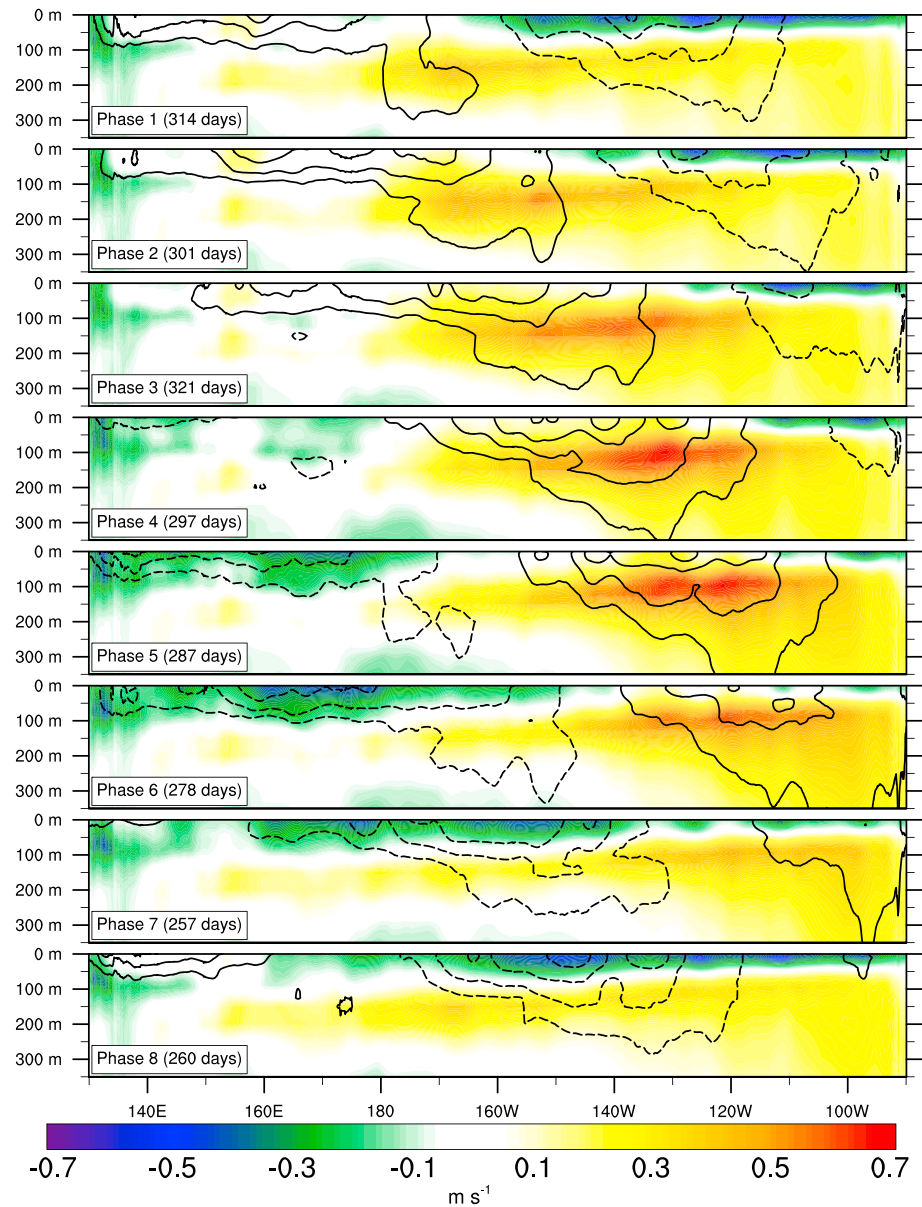


Figure 12. Composites of 30–120-day band-pass-filtered Hybrid Coordinate Ocean Model zonal velocity anomalies (line contours, m/s) and total Hybrid Coordinate Ocean Model zonal velocity (shading, m/s) based on the Kelvin wave index are shown for phases 1–8. Velocities are averaged from 2°S–2°N. The number of days in each composite is shown in the bottom left. The intraseasonal velocity contour interval is 0.05 m/s with the zero contour line omitted. Positive (negative) contours are solid (dashed).

McCreary, 1993; Kutsuwada & McPhaden, 2002; Lukas & Firing, 1984). While the intraseasonal currents maximize at the ocean surface with values of ± 0.4 m/s, important impacts are noted in the equatorial undercurrent. The maximum of upper ocean total currents (shading) is located between 50 and 150 m from 180–100°W with the maximum ranging from 0.38–0.67 m/s depending on the IKW phase. The total current maximum propagates eastward consistent with the eastward propagation of the intraseasonal currents, indicating a modulating effect of the total currents by the IKW. The undercurrent maximum shifts $\sim 3,500$ km to the east in 35 days (from phase 2 to phase 5) and ascends in the water column toward the east Pacific, following the slope of the thermocline (see also Figure 13). The intraseasonal currents are strong enough to reverse the sign of the total zonal flow in the ocean's upper 50 m (Figure 12) at 170°W (from phase 7 to phase 3) and 135°W (from phase 1 to phase 5).

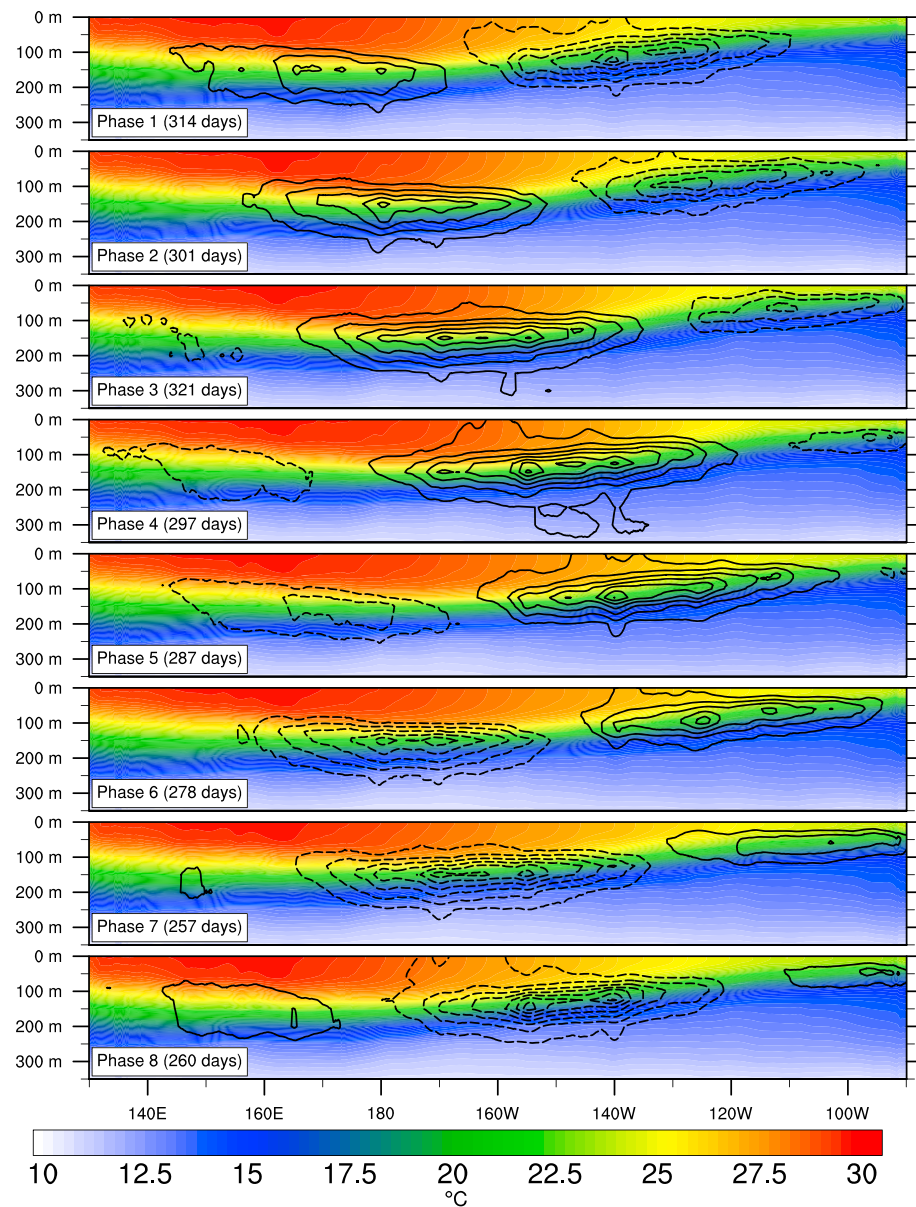


Figure 13. Composites of 30–120-day band-pass-filtered Hybrid Coordinate Ocean Model temperature anomalies (line contours, m/s) and total Hybrid Coordinate Ocean Model temperature (shading, m/s) based on the Kelvin wave index are shown for phases 1–8. Temperatures are averaged from 2°S–2°N. The number of days in each composite is shown in the bottom left. The intraseasonal temperature contour interval is 0.2 °C with the zero contour line omitted. Positive (negative) contours are solid (dashed).

Next, we examine the total temperature and intraseasonal temperature anomalies in the thermocline (Figure 13). Maxima and minima of intraseasonal temperature anomalies propagate along the thermocline from west to east, reaching their greatest amplitude of ± 1.4 °C near 155°W (phases 4 and 8, respectively). The anomalies follow the upslope of the thermocline in the east Pacific while gradually weakening east of 155°W. The surface warming, when present, lags the warm maximum along the thermocline. The intraseasonal temperature anomaly maximum is reduced by 57% to 0.6 °C when it arrives in the east Pacific (phase 7) compared to its peak in phase 4. Although the temperature anomalies are reduced in the east Pacific, their effect of depressing the thermocline still has important consequences for local air-sea interactions, such as increased resiliency to surface cooling by wind-driven mixing associated with atmospheric convection. An

important but subtle consequence of IKWs is a zonal shift of the ocean warm pool indicated by SST. The warm pool ($>27^\circ\text{C}$) shifts eastward during downwelling IKWs and westward during upwelling IKWs, resulting in a 1,700-km displacement between phases 1 and 6. Zonal shifts of the west Pacific warm pool have important consequences for the extent of zonal propagation of convectively driven atmospheric phenomenon such as the MJO (e.g., Hendon et al., 1999; Kessler & Kleeman, 2000; Pohl & Matthew, 2007; Slingo et al., 1999).

4.3. Mixed-Layer Heat Budget

Previous studies (e.g., McPhaden, 2002; Zhang, 2001) have observed that the phase relationship between the IKW and the mixed-layer/surface temperature anomalies varies across the Pacific Ocean. Using the Tropical Atmosphere Ocean array of moored buoys, McPhaden (2002) determined that the leading processes of intraseasonal mixed-layer variability are surface fluxes in the western Pacific, zonal advection in the central Pacific, and vertical advection and mixing in the east Pacific. Zhang (2001) observed both eastward and westward propagations of intraseasonal temperature anomalies, suggesting competing roles among processes regulating the temperature. These processes are reexamined using HYCOM reanalysis to determine the regimes of mixed-layer temperature tendency variations along the equatorial Pacific Ocean *during particular phases of IKWs*, a distinguishing aspect of this study.

The mixed-layer temperature budget (Moisan & Niiler, 2002; Scannell & McPhaden, 2018; Stevenson & Niiler, 2002) may be expressed as

$$\left(\frac{\partial MLT}{\partial t}\right)' = -(U \cdot \nabla MLT)' + (Q_s)' + R, \quad (5)$$

where $\frac{\partial}{\partial t}$ is the local time tendency, MLT is the vertically averaged mixed-layer temperature, U is the vertically averaged mixed-layer horizontal velocity, Q_s is the net surface fluxes that are scaled by the mixed-layer depth and volumetric heat capacity of seawater, and R is the residual. Primed terms are calculated as 30–120-day band-pass-filtered anomalies. The net surface fluxes include latent heat, sensible heat, longwave radiative, and net shortwave radiative fluxes. The net shortwave radiative flux is calculated as the incoming shortwave radiative flux less the flux that penetrates the base of the mixed layer, as in Pacanowski and Griffies (2000). The fraction of shortwave radiation that penetrates the mixed layer is defined as $f_{sr} = 0.58e^{-MLD/0.35m} + (1-0.58)e^{-MLD/23m}$. The mixed-layer depth is calculated using HYCOM/NCODA reanalysis data, and the fixed density criterion of 0.125 kg/m^3 referenced from the surface (e.g., Levitus, 1982). Surface fluxes from the National Centers for Environmental Prediction Climate Forecast System Reanalysis that are used to force the HYCOM/NCODA are also utilized in the flux calculations of the mixed-layer temperature budget. The residual, R , includes processes not resolved in the budget, notably vertical advection and mixing (Foltz, 2003; Scannell & McPhaden, 2018). It also includes analysis increments from NCODA and any errors in the calculation of other budget terms. The intraseasonal mixed-layer temperature tendency, $\left(\frac{\partial MLT}{\partial t}\right)'$, is forced by the horizontal advection, $-(U \cdot \nabla MLT)'$, net surface fluxes, $(Q_s)'$, and the residual, R .

Terms of the intraseasonal mixed-layer heat budget composited for IKWs and averaged from 1°S – 1°N are shown in Figure 14. The mixed-layer temperature tendency (Figure 14a) shows a coherent eastward propagating signal across much of the Pacific Ocean. The filled black circles approximate the location of the downwelling Kelvin wave. The intraseasonal warming tendency (shading) leads the Kelvin wave by one phase (~ 8 days), while warm intraseasonal SST anomalies (contours) lag by one phase. Thus, the warming tendency generally occurs on the leading edge of the wave, and the warm anomalies manifest on the trailing edge. The maximum warming tendency occurs near 160°W with a value above 0.21°C/week and corresponds to a mixed-layer temperature maximum of 0.24°C ~ 18 days later at the same location. A comparable mixed-layer temperature maximum is also present between 150°W and 135°W . East of 120°W , the eastward propagation of MLT tendency and MLT anomalies is less coherent.

The components of the mixed-layer temperature budget are also shown in Figure 14. Components of the budget that are in phase (out of phase) with the MLT maxima/minima at a particular longitude contribute to their strengthening (weakening) and those that are 90° out of phase contribute to the propagation of

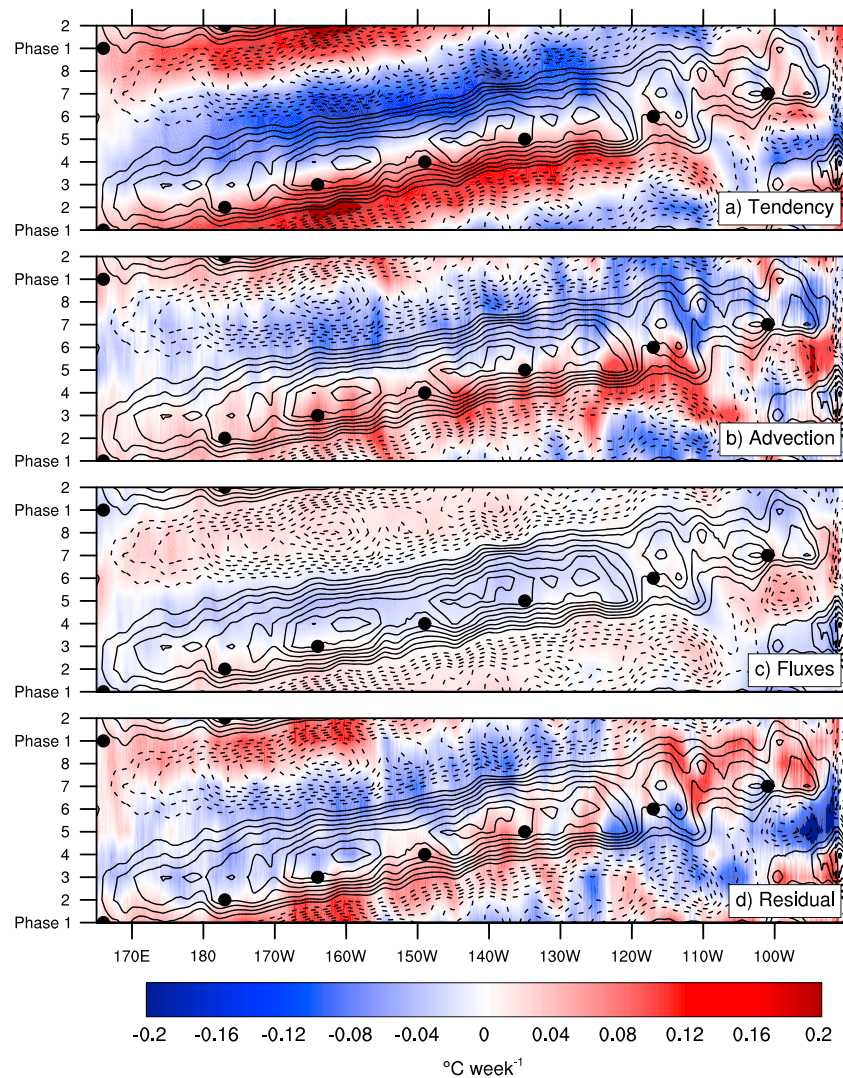


Figure 14. Composites of the intraseasonal mixed-layer temperature budget averaged from 1°S–1°N are shown. The (a) mixed-layer temperature tendency, (b) mixed-layer advection, (c) scaled net surface fluxes, and (d) residual terms of the budget are shown in shading ($^{\circ}\text{C}/\text{week}$). The intraseasonal mixed-layer temperature anomalies are shown in line contours ($^{\circ}\text{C}$). The intraseasonal temperature contour interval is 0.03°C with the zero contour line omitted. Positive (negative) contours are solid (dashed). Black dots indicate the approximate location of the downwelling Kelvin wave.

maxima/minima. In the west Pacific Ocean, the phase relationship of horizontal advection (shading) and the intraseasonal MLT (contour) anomalies subtly shifts as the downwelling wave propagates from the west to east Pacific Ocean (Figure 14b). In the west Pacific, warming by horizontal advection leads and overlaps the temperature maxima, indicating that advection both assists the eastward propagation and intensification of warm anomalies. The phase relationship between horizontal advection and the warm SST anomalies changes east of 150°W where warming by horizontal advection no longer overlaps with the mixed-layer temperature maxima indicating that intensification of MLT anomalies by advection has ceased. Zonal advection dominates the horizontal advection term in the western and central Pacific. In certain regions east of 150°W , advection contributes to a modest cooling of the warm MLT maxima. This is particularly noteworthy in the east Pacific near 110°W and 95°W where the role of meridional advection features more prominently (respective zonal and meridional advectons not shown).

The intraseasonal mixed-layer temperature tendency resulting from surface fluxes is shown in Figure 14c. The phase relationship between the flux tendency and the MLT anomalies remains consistent across

much of the Pacific Ocean. The fluxes and MLT anomalies are predominantly out of phase, indicating that the leading role of surface fluxes is to suppress IKW MLT anomalies. Exceptions to this occur near 175°E–175°W and in select regions east of 120°W where surface fluxes assist the propagation of MLT anomalies. The tendency from fluxes is the weakest contributor to the MLT tendency with values between 0.01 and 0.05 °C/week over much of the basin. These are generally an order of magnitude lower than the other terms of the MLT budget. McPhaden (2002) showed an important role for local surface fluxes to intraseasonal temperature variability in the west Pacific Ocean. Our results do not diminish those findings but rather suggest surface fluxes *during active periods of IKWs in the west Pacific* contribute to a dampening of MLT anomalies. While the role of surface fluxes in the present analysis is minor, the coherent propagation of the MLT anomalies and MLT tendency by surface fluxes is curious. One possibility might be related to coupling between atmospheric intraseasonal convection and oceanic Kelvin waves wherein convection reduces incoming solar radiation along the path of IKWs (i.e., Gribble-Verhagen & Roundy, 2010; Roundy & Gribble-Verhagen, 2010).

The residual, which includes contributions from vertical advection and mixing, exhibits a subtle phase shift across the Pacific that incompletely opposes the strengthening and weakening of MLT anomalies resulting from horizontal advection (Figure 14d). The residual cools warm MLT anomalies in the west and central Pacific Ocean and fortifies warm MLT anomalies in much of the east Pacific. The residual maximum of +0.2 °C/week is located at 95°W with secondary maxima of +0.15 °C/week located at 115°W and 110°W. Anomalous warming due to vertical advection and mixing is expected in the east Pacific owing to the deepening of the thermocline and increasing of the thermal stratification by downwelling IKWs. Warming by the residual near 95°W and 100°W is almost entirely in phase with the warm MLT anomalies such that the residual contributes most to the intensification of the anomalies and relatively little to their propagation. Because the tendencies from horizontal advection and surface fluxes attempt to cool the MLT at these locations, processes contained within the residual are almost entirely responsible for the intensification of warm MLT anomalies there.

In summary, intraseasonal MLT temperature anomalies are supported by various process across the Pacific Ocean, in general agreement with the findings of earlier studies. Our investigation differs from previous analyses in that we focus on the intraseasonal MLT tendencies forced by Kelvin waves. Near 175°E, MLT anomalies develop in response to horizontal advection of which zonal advection is the leading contributor. Warming by horizontal advection is incompletely opposed by the net surface flux and residual which act to cool the west and central Pacific mixed layer during downwelling Kelvin waves. Near 150°W, a regime change occurs. The principle process of MLT warming to the east of 150°W is embedded within the residual term, and horizontal advection, with weak assistance from surface fluxes, dampens warm MLT anomalies. Drawing on the conclusions of previous studies (i.e., McPhaden, 2002; Zhang, 2001), we hypothesize that the leading processes within the residual are vertical advection and mixing. Thus, the local MLT maxima near 160°W are forced by horizontal advection, and the local maxima near 140°W are forced by processes contained within the residual term. Local maxima in the far east Pacific are almost entirely forced by the residual, in opposition to strong damping by horizontal advection.

5. Modulation of Kelvin Waves by ENSO

Background oceanic and atmospheric states have demonstrated considerable control over the phase speed, magnitude, frequency, and surface presentation of IKWs. In order to better understand these sensitivities, IKWs are composited based on the chief mode of equatorial interannual variability in the Pacific, the ENSO. To understand the differences in atmospheric forcing between El Niño and La Niña, composites of intraseasonal SSH and zonal pseudostress anomalies are shown for the respective ENSO states (Figures 15 and 16). The IKW index threshold for compositing is reduced to 1.0 in order to include a representative sample size for all ENSO states. The La Niña composite includes 45% fewer days than the El Niño composite, indicating reduced number of qualifying IKW events (see also Figure 17).

Compared to El Niño (Figure 15), zonal pseudostress anomalies during La Niña (Figure 16) are less persistent and more confined to the West Pacific. The pseudostress anomalies are, on average, weaker during La Niña but that is not always the case as evidenced by comparing phase 8 of Figures 15 and 16. The

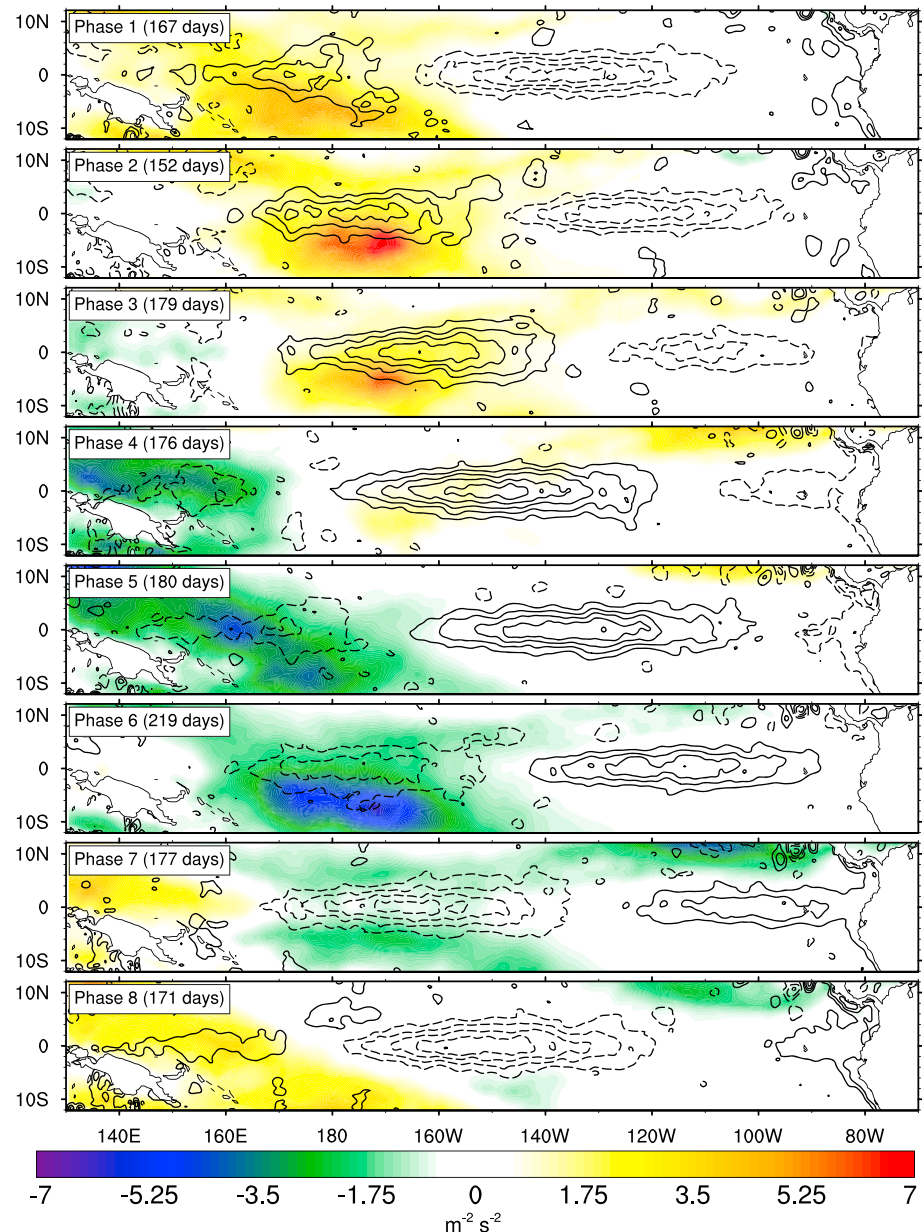


Figure 15. Composites of 30–120-day band-pass-filtered sea surface height (line contours, cm) and European Centre for Medium-Range Weather Forecasts Interim Reanalysis zonal pseudostress (shading, $\text{m}^{-2} \text{s}^{-2}$) anomalies based on the Kelvin wave index are shown for phases 1–8 for waves occurring during El Niño. The number of days in each composite is shown in the upper left. The sea surface height contour interval is 1 cm with the zero contour line omitted. Positive (negative) contours are solid (dashed).

pseudostress anomalies are notably weaker near the date line during La Niña, when Kelvin waves are typically intensifying and approximately 2–3 weeks prior to Kelvin wave peak intensity. Westerly wind events, such as the MJO, are well known to display sensitivity to low-frequency interannual variability such as ENSO (e.g., Gutzler, 1991; Hendon et al., 2007; W. S. Kessler, 2001; Lau, 2005; Pohl & Matthew, 2007; Vecchi & Harrison, 2000; Woolnough et al., 2000) and may be responsible for the observed changes in wind forcing. For example, Kessler (2001) and Pohl and Matthew (2007) observed an eastward extension of MJO activity over the Pacific Ocean during El Niño suggesting a greater fetch of wind stress forcing.

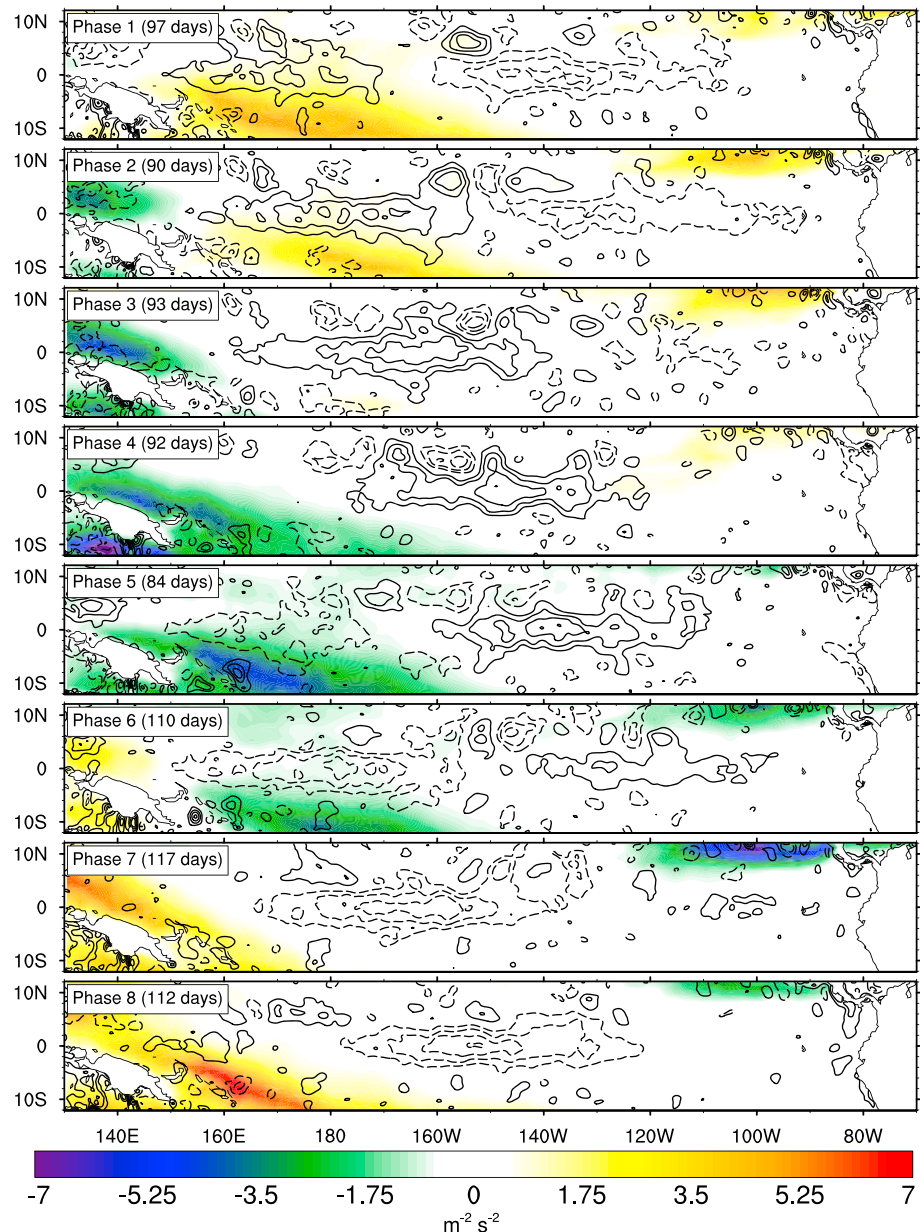


Figure 16. Composites of 30–120-day band-pass-filtered sea surface height (line contours, cm) and European Centre for Medium-Range Weather Forecasts Interim Reanalysis zonal pseudostress (shading, $\text{m}^{-2} \text{s}^{-2}$) anomalies based on the Kelvin wave index are shown for phases 1–8 for waves occurring during La Niña. The number of days in each composite is shown in the upper left. The sea surface height contour interval is 1 cm with the zero contour line omitted. Positive (negative) contours are solid (dashed).

The weaker pseudostress during the growth stages of downwelling Kelvin waves is associated with a weaker oceanic response as evidenced by intraseasonal SSH anomalies (contours) that are reduced by 20–40% in phases 3 and 4 compared to SSH anomalies for similar phases during El Niño. Maxima and minima of pseudostress are also slightly shifted more poleward during La Niña (phases 1 and 2), somewhat limiting their oceanic forcing along the equator. The SSH anomalies rapidly weaken over the central Pacific, terminating before reaching the eastern boundary. This behavior is contrasted by IKWs during El Niño that coherently propagate across the entire basin. Like the SSH anomalies, subsurface temperature anomalies propagate across the entire basin only during El Niño (figures not shown). This translates to greater and more coherent propagation of OHC anomalies across the basin during El Niño.

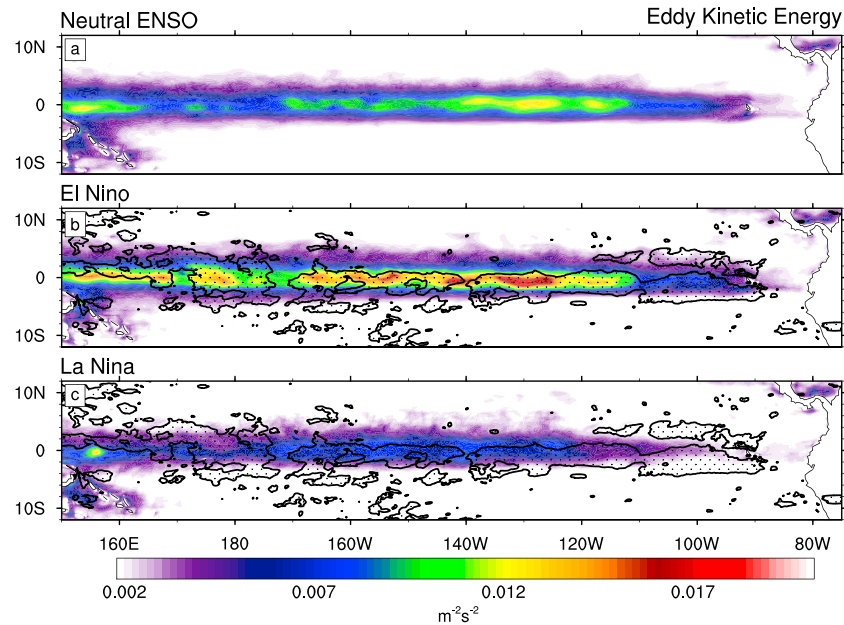


Figure 17. Composites of eastward wave number and 30–120-day band-pass-filtered Hybrid Coordinate Ocean Model eddy kinetic energy ($\text{m}^{-2} \text{s}^{-2}$) are shown. EKE is composited during periods when the Kelvin wave index is greater than 1.0 and for (a) neutral ENSO conditions, (b) El Niño events, and (c) La Niña events. Statistically significant differences between the El Niño and La Niña eddy kinetic energies at the 99% threshold according to the two-tailed Welch's t test are overlaid with stippling and outlined by a solid black contour line. ENSO = El Niño Southern Oscillation.

To quantify differences in Kelvin wave activity as a function of the ENSO state, a form of eddy kinetic energy is calculated that isolates signals associated with IKWs. The eddy kinetic energy is calculated using surface currents from HYCOM reanalysis following the formula:

$$EKE_{KW} = \left[\frac{1}{2} (\overline{U'^2} + \overline{V'^2}) \right]_{k>0}, \quad (6)$$

where primes indicate 30–120-day band-pass-filtered anomalies and the overbars indicate the 120-day running mean. The EKE for IKWs is further isolated by filtering the currents in wave number space to remove westward propagating variability, such as tropical instability waves, that are retained in the frequency filtering and complicate the interpretation. The EKE composite for the respective ENSO states only includes those times when the IKW index is greater than 1.0.

The IKW kinetic energies during neutral ENSO (Figure 17a), El Niño (Figure 17b), and La Niña (Figure 17c) periods are shown. During neutral ENSO periods, IKW kinetic energy broadly maximizes in two distinct regions, 150–160°E and 140–115°W, and is largely bound along the equator between 5°S and 5°N. The western Pacific Ocean maximum is located in a region of strong intraseasonal zonal pseudostress variance (see Figure 11) and corresponds to longitudes of Kelvin wave generation. The strong wind forcing corresponds to intense near-surface currents even though the Kelvin wave is nascent (see Figure 12) and SSH anomalies are modest (see Figures 8 and 13). The second maximum in the east Pacific Ocean extends over a greater zonal distance and corresponds to longitudes where pseudostress is weak and the wave is propagating freely. This is a region where the surface currents used to calculate the eddy kinetic energy are almost entirely determined by the Kelvin wave activity, not direct wind forcing, and occurs prior to the region of greatest thermocline upslope (see Figure 13).

During El Niño, Kelvin wave kinetic energy maxima increase by ~40% compared to maxima during neutral ENSO, with even greater increases in the central Pacific Ocean (Figure 17b). Kelvin wave kinetic energy during El Niño is generally increased everywhere along the path of wave propagation, except in the east Pacific between 110°W and 85°W where the energy is mostly unchanged. IKW activity during La Niña is generally

weaker everywhere across the Pacific compared to neutral ENSO and El Niño. Regions where IKW kinetic energy differences between the El Niño and La Niña are significant at the 99% significance level using the two-tailed Welch's t test are overlaid with stippling. Statistically significant differences span much of the equatorial waveguide. In addition to being a well-documented instigator of ENSO variability, these results suggest that Kelvin wave activity is also significantly modulated by ENSO.

6. Conclusions

A methodology for identifying IKWs in the Pacific Ocean is developed to examine the wave's horizontal and vertical structures as well as its evolution from inception to termination. The methodology is based on satellite-derived SSH anomalies. The anomalies are filtered in wave number-frequency space to isolate eastward-propagating intraseasonal signals. The two leading EOFs of this data describe an eastward-propagating IKW and are used to develop indices that define wave amplitude and phase. A key benefit of this methodology is the ability to probe previous IKW events. A complementary IKW index is developed for describing events in real time. The PCs of the real-time IKW index are highly correlated with those of the IKW index (0.87 and 0.86). Composites based on the IKW index are analyzed to evaluate the salient features of waves as they transit the Pacific Ocean.

The average phase speed of IKWs using this methodology is 2.55 m/s, with a maximum phase speed of 2.73 m/s when the downwelling portion of the wave is located at 150°W. IKWs reach their maximum SSH amplitude at 150°W and shift from a forced wave to a freely propagating wave at this longitude as well. IKW SSH anomalies and surface currents gradually weaken when the wave becomes a free mode. Maxima (minima) of SST anomalies associated with downwelling (upwelling) waves generally lag maxima (minima) of SSH. Intraseasonal SST anomalies associated with the waves have a maximum magnitude of 0.25 °C. The phase relationship between MLT and SSH anomalies evolves as the waves propagate eastward as a result of competition among processes controlling the temperature tendency. This is observed in the mixed-layer temperature budget, wherein horizontal advection is largely responsible for warming in the west and central Pacific and the residual, which includes vertical advection and mixing, is almost entirely responsible for warming in the east Pacific. The change between warming regimes occurs around 150°W, the location where mean zonal temperature gradients begin to relax. Surface fluxes play a secondary role in the MLT tendency of IKWs and generally oppose the MLT anomalies such that warm (cold) anomalies are cooled (warmed).

Temperature anomalies along the thermocline are much stronger than at the surface, with maximum amplitude of ± 1.4 °C, corresponding to a 2.8 °C temperature displacement in a period of 70 days. IKWs also intensify the equatorial undercurrent by up to 76% (from 0.38–0.67 m/s) and shift the maximum eastward by $\sim 3,500$ km over a 35-day period. In certain regions (170°W and 135°W), the intraseasonal currents associated with the waves are able to reverse the total zonal flow of the ocean's upper 50 m.

ENSO strongly modulates Pacific IKW activity, with statistically significant decreases of IKW kinetic energy over much of the equatorial Pacific during La Niña versus El Niño. This is partly a result of the reduced intensity and duration of westerly zonal wind forcing observed during La Niña that results in a weaker and less coherent oceanic response. Kelvin waves during La Niña wane much more quickly along their eastward transit with little SSH signal reaching the eastern edge of the Pacific basin, unlike Kelvin waves during neutral ENSO and El Niño.

The establishment of an objective framework for analyzing IKWs in the Pacific has considerable utility that is briefly leveraged in this study. The real-time IKW index derived from satellite observations can be compared with that forecasted by deterministic and ensemble oceanic models to calculate model skill scores for IKWs in the Pacific. This methodology also provides a basis for intermodel comparisons of oceanic intraseasonal variability, which is already commonly done for atmospheric intraseasonal variability. The IKW index may also be used to analyze IKWs as a function of season and other modes of interannual variability such as the Indian Ocean Dipole. Future work includes plans to perform lag analyses based on particular IKW phases to better tease out the sensitivity of IKW development to the behavior of the westerly wind forcing, including the forcing's origin, time scale, strength, propagation pattern, and associated convective activity.

Acknowledgments

The authors would like to thank two anonymous reviewers whose comments greatly improved the manuscript. Financial support for A. V. R. is provided by the NRL Karle's Fellowship, T. G. J. by the U.S. Office of Naval Research Directed Research Initiative, PISTON (73-4347-27-5), and M. F. by the Naval Research Laboratory Base Program PE0601153N. SSHs are produced by Ssalto/Duacs and distributed by AVISO, with support from CNES (<http://www.aviso.altimetry.fr/duacs/>). NOAA SST is provided by the NCEI (<http://www.ncdc.noaa.gov/oisst>). OSCAR currents are produced by ESR and hosted by JPL PODAAC (http://www.esr.org/oscar_index.html). ERAi Reanalysis is provided by ECMWF (<http://apps.ecmwf.int/datasets/>). HYCOM + NCOA Reanalysis is stored at the Navy DoD Supercomputing Resource Center (DSRC). Access to the DSRC may be obtained through a request to the DoD High Performance Computer Modernization Program (<https://www.hpc.mil/>). Once an account has been established, the corresponding author may be contacted for information to access the archived data.

References

- Batstone, C., & Hendon, H. H. (2005). Characteristics of stochastic variability associated with ENSO and the role of the MJO. *Journal of Climate*, *18*(11), 1773–1789. <https://doi.org/10.1175/JCLI3374.1>
- Benestad, R. E., Sutton, R. T., & Anderson, D. L. T. (2002). The effect of El Niño on intraseasonal Kelvin waves. *Quarterly Journal of the Royal Meteorological Society*, *128*(582), 1277–1291. <https://doi.org/10.1256/003590002320373292>
- Bergman, J. W., Hendon, H. H., & Weickmann, K. M. (2001). Intraseasonal air-sea interaction at the onset of El Niño. *Journal of Climate*, *14*(8), 1702–1719. [https://doi.org/10.1175/1520-0442\(2001\)014<1702:IASIAT>2.0.CO;2](https://doi.org/10.1175/1520-0442(2001)014<1702:IASIAT>2.0.CO;2)
- Bjerknes, J. (1969). Atmospheric teleconnections from the equatorial Pacific¹. *Monthly Weather Review*, *97*(3), 163–172. [http://doi.org/10.1175/1520-0493\(1969\)097<0163:ATFTEP>2.3.CO;2](http://doi.org/10.1175/1520-0493(1969)097<0163:ATFTEP>2.3.CO;2)
- Bleck, R. (2002). An oceanic general circulation model framed in hybrid isopycnic-Cartesian coordinates. *Ocean Modelling*, *4*(1), 55–88. [https://doi.org/10.1016/S1463-5003\(01\)00012-9](https://doi.org/10.1016/S1463-5003(01)00012-9)
- Bonjean, F., & Lagerloef, G. S. E. (2002). Diagnostic model and analysis of the surface currents in the tropical Pacific Ocean. *Journal of Physical Oceanography*, *32*(10), 2938–2954. [https://doi.org/10.1175/1520-0485\(2002\)032<2938:DMAAOT>2.0.CO;2](https://doi.org/10.1175/1520-0485(2002)032<2938:DMAAOT>2.0.CO;2)
- Boucharel, J., Jin, F. F., England, M. H., Dewitte, B., Lin, I. I., Huang, H. C., & Balmaseda, M. A. (2016). Influence of oceanic intraseasonal Kelvin waves on eastern Pacific hurricane activity. *Journal of Climate*, *29*(22), 7941–7955. <https://doi.org/10.1175/JCLI-D-16-0112.1>
- Boulanger, J.-P., & Menkes, C. (1995). Propagation and reflection of long equatorial waves in the Pacific Ocean during the 1992–1993 El Niño. *Journal of Geophysical Research*, *100*(C12), 25041. <https://doi.org/10.1029/95JC02956>
- Busalacchi, A. J., & Cane, M. A. (1988). The effect of varying stratification on low-frequency equatorial motions. *Journal of Physical Oceanography*, *18*(6), 801–812. [https://doi.org/10.1175/1520-0485\(1988\)018<0801:TEOVSO>2.0.CO;2](https://doi.org/10.1175/1520-0485(1988)018<0801:TEOVSO>2.0.CO;2)
- Busalacchi, A. J., Takeuchi, K., & O'Brien, J. J. (1983). Interannual variability of the equatorial Pacific—Revisited. *Journal of Geophysical Research*, *88*(C12), 7551–7562. <https://doi.org/10.1029/JC088C12p07551>
- Chassignet, E. P., Smith, L. T., Halliwell, G. R., & Bleck, R. (2003). North Atlantic simulations with the Hybrid Coordinate Ocean Model (HYCOM): Impact of the vertical coordinate choice, reference pressure, and thermobaricity. *Journal of Physical Oceanography*, *33*(12), 2504–2526. [https://doi.org/10.1175/1520-0485\(2003\)033<2504:NASWTH>2.0.CO;2](https://doi.org/10.1175/1520-0485(2003)033<2504:NASWTH>2.0.CO;2)
- Chelton, D. B., DeSzoeke, R. A., Schlax, M. G., El Naggar, K., & Siwertz, N. (1998). Geographical variability of the first baroclinic Rossby radius of deformation. *Journal of Physical Oceanography*, *28*(3), 433–460. [https://doi.org/10.1175/1520-0485\(1998\)028<0433:GVOTFB>2.0.CO;2](https://doi.org/10.1175/1520-0485(1998)028<0433:GVOTFB>2.0.CO;2)
- Cravatte, S. (2003). Second and first baroclinic Kelvin modes in the equatorial Pacific at intraseasonal timescales. *Journal of Geophysical Research*, *108*(C8), 3266. <http://doi.org/10.1029/2002JC001511>
- Cummings, J. A. (2006). Operational multivariate ocean data assimilation. *Quarterly Journal of the Royal Meteorological Society*, *131*(613), 3583–3604. <http://doi.org/10.1256/qj.05.105>
- Cummings, J. A., & Smedstad, O. M. (2013). Variational data assimilation for the global ocean. In *Data assimilation for atmospheric, oceanic and hydrologic applications* (Vol. II, pp. 303–343). Berlin, Heidelberg: Springer Berlin Heidelberg. http://doi.org/10.1007/978-3-642-35088-7_13
- Dee, D. P., Uppala, S. M., Simmons, A. J., Berrisford, P., Poli, P., Kobayashi, S., et al. (2011). The ERA-Interim reanalysis: Configuration and performance of the data assimilation system. *Quarterly Journal of the Royal Meteorological Society*, *137*(656), 553–597. <https://doi.org/10.1002/qj.828>
- Dewitte, B., Purca, S., Illig, S., Renault, L., & Giese, B. S. (2008). Low-frequency modulation of intraseasonal equatorial Kelvin wave activity in the Pacific from SODA: 1958–2001. *Journal of Climate*, *21*(22), 6060–6069. <https://doi.org/10.1175/2008JCLI2277.1>
- Enfield, D. B., Cornejo-Rodriguez, M. D. P., Smith, R. L., & Newberger, P. A. (1987). The equatorial source of propagating variability along the Peru coast during the 1982–1983 El Niño. *Journal of Geophysical Research*, *92*(C13), 14335. <http://doi.org/10.1029/JC092iC13p14335>
- Eriksen, C. C., Blumenthal, M. B., Hayes, S. P., & Ripa, P. (1983). Wind-generated equatorial Kelvin waves observed across the Pacific Ocean. *Journal of Physical Oceanography*, *13*(9), 1622–1640. [https://doi.org/10.1175/1520-0485\(1983\)013<1622:WGEKWO>2.0.CO;2](https://doi.org/10.1175/1520-0485(1983)013<1622:WGEKWO>2.0.CO;2)
- Eriksen, C. C., & Richman, J. G. (1988). An estimate of equatorial wave energy flux at 9- to 90-day periods in the Central Pacific. *Journal of Geophysical Research*, *93*(C12), 15,455–15,466. <https://doi.org/10.1029/JC093iC12p15455>
- ESR. (2009). OSCAR third degree resolution ocean surface currents. <http://doi.org/https://doi.org/10.5067/OSCAR-03D01>
- Farrar, J. T. (2008). Observations of the dispersion characteristics and meridional sea level structure of equatorial waves in the Pacific Ocean. *Journal of Physical Oceanography*, *38*(8), 1669–1689. <https://doi.org/10.1175/2007JPO3890.1>
- Feng, J., Wang, Q., Hu, S., & Hu, D. (2016). Intraseasonal variability of the tropical Pacific subsurface temperature in the two flavours of El Niño. *International Journal of Climatology*, *36*(2), 867–884. <https://doi.org/10.1002/joc.4389>
- Foltz, G. R. (2003). Seasonal mixed layer heat budget of the tropical Atlantic Ocean. *Journal of Geophysical Research*, *108*(C5), 3146. <https://doi.org/10.1029/2002JC001584>
- Fox, D. N., Teague, W. J., Barron, C. N., Carnes, M. R., & Lee, C. M. (2002). The modular ocean data assimilation system (MODAS). *Journal of Atmospheric and Oceanic Technology*, *19*(2), 240–252. [https://doi.org/10.1175/1520-0426\(2002\)019<0240:TMODAS>2.0.CO;2](https://doi.org/10.1175/1520-0426(2002)019<0240:TMODAS>2.0.CO;2)
- Gasparin, F., Roemmich, D., Gilson, J., & Cornuelle, B. (2015). Assessment of the upper-ocean observing system in the equatorial Pacific: The role of Argo in resolving intraseasonal to interannual variability. *Journal of Atmospheric and Oceanic Technology*, *32*(9), 1668–1688. <https://doi.org/10.1175/JTECH-D-14-00218.1>
- Giese, B. S., & Harrison, D. E. (1990). Aspects of the Kelvin wave response to episodic wind forcing. *Journal of Geophysical Research*, *95*(C5), 7289–7312. <https://doi.org/10.1029/JC095iC05p07289>
- Gribble-Verhagen, L., & Roundy, P. E. (2010). Analysis of apparent coupling between an oceanic Kelvin wave and atmospheric convection during the winter of 1986/87. *Journal of Climate*, *23*(23), 6352–6364. <https://doi.org/10.1175/2010JCLI3790.1>
- Gutzler, D. S. (1991). Interannual fluctuations of intraseasonal variance of near-equatorial zonal winds. *Journal of Geophysical Research*, *96*(S01), 3173. <http://doi.org/10.1029/90jd01831>
- Harrison, D. E., & Giese, B. S. (1988). Remote westerly wind forcing of the eastern equatorial Pacific; some model results. *Geophysical Research Letters*, *15*(8), 804–807. <https://doi.org/10.1029/GL015i008p00804>
- Harrison, D. E., & Schopf, P. S. (1984). Kelvin-wave-induced anomalous advection and the onset of surface warming in El Niño events. *Monthly Weather Review*, *112*(5), 923–933. [https://doi.org/10.1175/1520-0493\(1984\)112<0923:KWIAAA>2.0.CO;2](https://doi.org/10.1175/1520-0493(1984)112<0923:KWIAAA>2.0.CO;2)
- Hayes, S. P., & Halpern, D. (1984). Correlation of current and sea level in the eastern equatorial Pacific. *Journal of Physical Oceanography*, *14*(4), 811–824. [https://doi.org/10.1175/1520-0485\(1984\)014<0811:COCASL>2.0.CO;2](https://doi.org/10.1175/1520-0485(1984)014<0811:COCASL>2.0.CO;2)

- Helber, R. W., Townsend, T. L., Barron, C. N., Dastugue, J. M., & Carnes, M. R. (2013). Validation test report for the Improved Synthetic Ocean Profile (ISOP) System, *Part I: Synthetic Profile Methods and Algorithm*. Retrieved from <http://www.dtic.mil/docs/citations/ADA585251>
- Hendon, H. H., Liebmann, B., & Glick, J. D. (1998). Oceanic Kelvin waves and the Madden-Julian Oscillation. *Journal of the Atmospheric Sciences*, *55*(1), 88–101. [https://doi.org/10.1175/1520-0469\(1998\)055<0088:OKWATM>2.0.CO;2](https://doi.org/10.1175/1520-0469(1998)055<0088:OKWATM>2.0.CO;2)
- Hendon, H. H., Wheeler, M. C., & Zhang, C. (2007). Seasonal dependence of the MJO-ENSO relationship. *Journal of Climate*, *20*(3), 531–543. <https://doi.org/10.1175/JCLI4003.1>
- Hendon, H. H., Zhang, C., & Glick, J. D. (1999). Interannual variation of the Madden-Julian oscillation during austral summer. *Journal of Climate*, *12*(8 PART 2), 2538–2550. [http://doi.org/10.1175/1520-0442\(1999\)012<2538:IVOTMJ>2.0.CO;2](http://doi.org/10.1175/1520-0442(1999)012<2538:IVOTMJ>2.0.CO;2)
- Holmes, R. M., & Thomas, L. N. (2016). Modulation of tropical instability wave intensity by equatorial Kelvin waves. *Journal of Physical Oceanography*, *46*(9), 2623–2643. <https://doi.org/10.1175/JPO-D-16-0064.1>
- Johnson, E. S., & McPhaden, M. J. (1993). Structure of intraseasonal Kelvin waves in the equatorial Pacific Ocean. *Journal of Physical Oceanography*, *23*(4), 608–625. [https://doi.org/10.1175/1520-0485\(1993\)023<0608:SOIKWI>2.0.CO;2](https://doi.org/10.1175/1520-0485(1993)023<0608:SOIKWI>2.0.CO;2)
- Jolliff, J. K., & Smith, T. A. (2014). Biological modulation of upper ocean physics: Simulating the biothermal feedback effect in Monterey Bay, California. *Journal of Geophysical Research: Biogeosciences*, *119*, 703–721. <https://doi.org/10.1002/2013JG002522>
- Karnauskas, K. B. (2013). Can we distinguish canonical El Niño from Modoki? *Geophysical Research Letters*, *40*, 5246–5251. <https://doi.org/10.1002/grl.51007>
- Kessler, W. S. (2001). EOF representations of the Madden-Julian and its connection with ENSO. *Journal of Climate*, *14*(13), 3055–3061. [https://doi.org/10.1175/1520-0442\(2001\)014<3055:EROTMJ>2.0.CO;2](https://doi.org/10.1175/1520-0442(2001)014<3055:EROTMJ>2.0.CO;2)
- Kessler, W. S., & Kleeman, R. (2000). Rectification of the Madden-Julian Oscillation into the ENSO cycle. *Journal of Climate*, *13*(20), 3560–3575. [https://doi.org/10.1175/1520-0442\(2000\)013<3560:ROTMJO>2.0.CO;2](https://doi.org/10.1175/1520-0442(2000)013<3560:ROTMJO>2.0.CO;2)
- Kessler, W. S., & McCreary, J. P. (1993). The annual wind-driven Rossby wave in the subthermocline equatorial Pacific. *Journal of Physical Oceanography*, *23*(6), 1192–1207. [https://doi.org/10.1175/1520-0485\(1993\)023<1192:TAWDRW>2.0.CO;2](https://doi.org/10.1175/1520-0485(1993)023<1192:TAWDRW>2.0.CO;2)
- Kessler, W. S., & McPhaden, M. J. (1995). The 1991–1993 El Niño in the central Pacific. *Deep Sea Research Part II: Topical Studies in Oceanography*, *42*(2–3), 295–333. [https://doi.org/10.1016/0967-0645\(95\)00041-N](https://doi.org/10.1016/0967-0645(95)00041-N)
- Kessler, W. S., McPhaden, M. J., & Weickmann, K. M. (1995). Forcing of intraseasonal Kelvin waves in the equatorial Pacific. *Journal of Geophysical Research*, *100*(C6), 10613–10,631. <https://doi.org/10.1029/95JC00382>
- Kikuchi, K., Wang, B., & Kajikawa, Y. (2012). Bimodal representation of the tropical intraseasonal oscillation. *Climate Dynamics*, *38*(9–10), 1989–2000. <https://doi.org/10.1007/s00382-011-1159-1>
- Kiladis, G. N., Dias, J., Straub, K. H., Wheeler, M. C., Tulich, S. N., Kikuchi, K., et al. (2014). A comparison of OLR and circulation-based indices for tracking the MJO. *Monthly Weather Review*, *142*(5), 1697–1715. <https://doi.org/10.1175/MWR-D-13-00301.1>
- Kindle, J. C., & Phoebus, P. A. (1995). The ocean response to operational westerly wind bursts during the 1991–1992 El Niño. *Journal of Geophysical Research*, *100*(C3), 4893–4920. <https://doi.org/10.1029/94JC02392>
- Knox, R., & Halpern, D. (1982). Long range Kelvin wave propagation of transport variations in Pacific Ocean equatorial currents. *Journal of Marine Research*, *40*(Suppl), 329–339. Retrieved from https://www.researchgate.net/publication/240098977_Long_range_Kelvin_wave_propagation_of_transport_variations_in_Pacific_Ocean_equatorial_currents
- Kutsuwada, K., & McPhaden, M. (2002). Intraseasonal variations in the upper equatorial Pacific Ocean prior to and during the 1997–98 El Niño. *Journal of Physical Oceanography*, *32*(4), 1133–1149. [https://doi.org/10.1175/1520-0485\(2002\)032<1133:IVITUE>2.0.CO;2](https://doi.org/10.1175/1520-0485(2002)032<1133:IVITUE>2.0.CO;2)
- Lau, W. K.-M. (2005). El Niño Southern Oscillation connection. In *Intraseasonal variability in the atmosphere-ocean climate system* (pp. 271–305). Chichester: Springer. https://doi.org/10.1007/3-540-27250-X_9
- Lee, J. Y., Wang, B., Wheeler, M. C., Fu, X., Waliser, D. E., & Kang, I. S. (2013). Real-time multivariate indices for the boreal summer intraseasonal oscillation over the Asian summer monsoon region. *Climate Dynamics*, *40*(1–2), 493–509. <https://doi.org/10.1007/s00382-012-1544-4>
- Lengaigne, M., Boulanger, J. P., Menkes, C., Madec, G., Delecluse, P., Guilyardi, E., & Slingo, J. (2003). The March 1997 westerly wind event and the onset of the 1997/98 El Niño: Understanding the role of the atmospheric response. *Journal of Climate*, *16*(20), 3330–3343. [https://doi.org/10.1175/1520-0442\(2003\)016<3330:TMWWEA>2.0.CO;2](https://doi.org/10.1175/1520-0442(2003)016<3330:TMWWEA>2.0.CO;2)
- Lengaigne, M., Boulanger, J.-P., Menkes, C., Masson, S., Madec, G., & Delecluse, P. (2002). Ocean response to the March 1997 westerly wind event. *Journal of Geophysical Research*, *107*(C12), 8015. <http://doi.org/10.1029/2001JC000841>
- Lengaigne, M., Guilyardi, E., Boulanger, J. P., Menkes, C., Delecluse, P., Inness, P., et al. (2004). Triggering of El Niño by westerly wind events in a coupled general circulation model. *Climate Dynamics*, *23*(6), 601–620. <https://doi.org/10.1007/s00382-004-0457-2>
- Levitus, S. (1982). *Climatological atlas of the world ocean, NOAA Prof. Pap.*, (Vol. 13). Washington, DC: U.S. Govt. Printing Off.
- Liu, P., Zhang, Q., Zhang, C., Zhu, Y., Khairoutdinov, M., Kim, H.-M., et al. (2016). A revised real-time multivariate MJO index. *Monthly Weather Review*, *144*(2), 627–642. <https://doi.org/10.1175/MWR-D-15-0237.1>
- Long, B., & Chang, P. (1990, December). Propagation of an equatorial Kelvin wave in a varying thermocline. *Journal of Physical Oceanography*, *20*(12), 1826–1841. [http://doi.org/10.1175/1520-0485\(1990\)020<1826:POAEKW>2.0.CO;2](http://doi.org/10.1175/1520-0485(1990)020<1826:POAEKW>2.0.CO;2)
- Lukas, R., & Firing, E. (1984). The geostrophic balance of the Pacific equatorial undercurrent. *Deep Sea Research Part A, Oceanographic Research Papers*, *31*(1), 61–66. [http://doi.org/10.1016/0198-0149\(84\)90072-4](http://doi.org/10.1016/0198-0149(84)90072-4)
- Lukas, R., Hayes, S. P., & Wyrtki, K. (1984). Equatorial sea level response during the 1982–1983 El Niño. *Journal of Geophysical Research*, *89*(C6), 10425. <https://doi.org/10.1029/JC089iC06p10425>
- Luther, D. S., Harrison, D. E., & Knox, R. A. (1983). Zonal winds in the central equatorial Pacific and El Niño. *Science*, *222*(4621), 327–330. <https://doi.org/10.1126/science.222.4621.327>
- Matsuno, T. (1966). Quasi-geostrophic motions in the equatorial area. *Journal of the Meteorological Society of Japan Series II*, *44*(1), 25–43. http://doi.org/10.2151/jmsj1965.44.1_25
- Matthews, A. J., Singhruck, P., & Heywood, K. J. (2007). Deep ocean impact of a Madden-Julian oscillation observed by Argo floats. *Science*, *318*(5857), 1765–1769. <https://doi.org/10.1126/science.1147312>
- McPhaden, M. J. (1999). Genesis and evolution of the 1997–98 El Niño. *Science*, *283*(5404), 950–954. <http://doi.org/10.1126/science.283.5404.950>
- McPhaden, M. J. (2002). Mixed layer temperature balance on intraseasonal timescales in the equatorial Pacific Ocean. *Journal of Climate*, *15*(18), 2632–2647. [https://doi.org/10.1175/1520-0442\(2002\)015<2632:MLTBOI>2.0.CO;2](https://doi.org/10.1175/1520-0442(2002)015<2632:MLTBOI>2.0.CO;2)
- McPhaden, M. J., Bahr, F., Du Penhoat, Y., Firing, E., Hayes, S. P., Niiler, P. P., et al. (1992). The response of the western equatorial Pacific Ocean to westerly wind bursts during November 1989 to January 1990. *Journal of Geophysical Research*, *97*(C9), 14289. <http://doi.org/10.1029/92JC01197>

- McPhaden, M. J., Freitag, H. P., Hayes, S. P., Taft, B. A., Chen, Z., & Wyrki, K. (1988). The response of the equatorial Pacific Ocean to a westerly wind burst in May 1986. *Journal of Geophysical Research*, 93(C9), 10,589–10,603. <http://doi.org/10.1029/JC093iC09p10589>
- McPhaden, M. J., & Taft, B. A. (1988). Dynamics of seasonal and intraseasonal variability in the eastern equatorial Pacific. *Journal of Physical Oceanography*, 18(11), 1713–1732. [https://doi.org/10.1175/1520-0485\(1988\)018<1713:DOSAIV>2.0.CO;2](https://doi.org/10.1175/1520-0485(1988)018<1713:DOSAIV>2.0.CO;2)
- McPhaden, M. J., Timmermann, A., Widlansky, M. J., Balmaseda, M. A., & Stockdale, T. N. (2015). The curious case of the El Niño that never happened: A perspective from 40 years of progress in climate research and forecasting. *Bulletin of the American Meteorological Society*, 96(10), 1647–1665. <https://doi.org/10.1175/BAMS-D-14-00089.1>
- McPhaden, M. J., & Yu, X. (1999). Equatorial waves and the 1997–98 El Niño. *Geophysical Research Letters*, 26(19), 2961–2964. <https://doi.org/10.1029/1999GL004901>
- Metzger, E. J., Helber, R. W., Hogan, P. J., Posey, P. G., Thoppil, P. G., Townsend, T. L., et al. (2017). Global Ocean Forecast System 3.1 Validation Testing. Naval Research Laboratory Technical Report. Retrieved from <http://www.dtic.mil/docs/citations/AD1034517>
- Metzger, E. J., Smedstad, O. M., Thoppil, P. G., Hurlburt, H. E., Cummings, J. A., Wallcraft, A. J., et al. (2014). US Navy operational global ocean and Arctic ice prediction systems. *Oceanography*, 27(3), 32–43. <http://doi.org/https://doi.org/10.5670/oceanog.2014.66>
- Moisan, J. R., & Niiler, P. P. (2002). The seasonal heat budget of the North Pacific: Net heat flux and heat storage rates (1950–1990). *Journal of Physical Oceanography*, 28(3), 401–421. [http://doi.org/10.1175/1520-0485\(1998\)028<0401:tshbot>2.0.co;2](http://doi.org/10.1175/1520-0485(1998)028<0401:tshbot>2.0.co;2)
- Mosquera-Vásquez, K., Dewitte, B., & Illig, S. (2014). The Central Pacific El Niño intraseasonal Kelvin wave. *Journal of Geophysical Research: Oceans*, 119, 6605–6621. <https://doi.org/10.1002/2014JC010044>
- North, G. R., Bell, T. L., Cahalan, R. F., & Moeng, F. J. (1982). Sampling errors in the estimation of empirical orthogonal functions. *Monthly Weather Review*, 110(7), 699–706. [https://doi.org/10.1175/1520-0493\(1982\)110<0699:SEITEO>2.0.CO;2](https://doi.org/10.1175/1520-0493(1982)110<0699:SEITEO>2.0.CO;2)
- Pacanowski, R. C., & Griffies, S. (2000). MOM 3.0 manual. Retrieved from http://www.mom-ocean.science/web/docs/project/MOM3_manual.pdf
- Pascual, A., Faugère, Y., Larnicol, G., & Le Traon, P. Y. (2006). Improved description of the ocean mesoscale variability by combining four satellite altimeters. *Geophysical Research Letters*, 33, L02611. <http://doi.org/10.1029/2005GL024633>
- Pohl, B., & Matthew, A. J. (2007). Observed changes in the lifetime and amplitude of the Madden-Julian oscillation associated with interannual ENSO sea surface temperature anomalies. *Journal of Climate*, 20(11), 2659–2674. <https://doi.org/10.1175/JCLI4230.1>
- Puy, M., Vialard, J., Lengaigne, M., Guilyardi, E., Voltaire, A., & Madec, G. (2016). Modulation of equatorial Pacific sea surface temperature response to westerly wind events by the oceanic background state. In *Climate dynamics* (pp. 1–25). Berlin, Heidelberg: Springer. <http://doi.org/10.1007/s00382-016-3480-1>
- Reynolds, R. W., Smith, T. M., Liu, C., Chelton, D. B., Casey, K. S., & Schlax, M. G. (2007). Daily High-Resolution-Blended Analyses for Sea Surface Temperature. *Journal of Climate*, 20, 5473–5496. <https://doi.org/10.1175/2007JCLI1824.1>
- Roundy, P. E., & Gribble-Verhagen, L. M. (2010). Variations in the flow of the global atmosphere associated with a composite convectively coupled oceanic Kelvin wave. *Journal of Climate*, 23(15), 4192–4201. <https://doi.org/10.1175/2010JCLI3630.1>
- Roundy, P. E., & Kiladis, G. N. (2006). Observed relationships between oceanic Kelvin waves and atmospheric forcing. *Journal of Climate*, 19(20), 5253–5272. <https://doi.org/10.1175/JCLI3893.1>
- Roundy, P. E., & Kiladis, G. N. (2007). Analysis of a reconstructed oceanic Kelvin wave dynamic height dataset for the period 1974–2005. *Journal of Climate*, 20(17), 4341–4355. <https://doi.org/10.1175/JCLI4249.1>
- Saha, S., Moorthi, S., Pan, H. L., Wu, X., Wang, J., Nadiga, S., et al. (2010). The NCEP climate forecast system reanalysis. *Bulletin of the American Meteorological Society*, 91(8), 1015–1058. <https://doi.org/10.1175/2010BAMS3001.1>
- Scannell, H. A., & McPhaden, M. J. (2018). Seasonal mixed layer temperature balance in the southeastern tropical Atlantic. *Journal of Geophysical Research: Oceans*, 123, 5557–5570. <https://doi.org/10.1029/2018JC014099>
- Schopf, P. S., & Harrison, D. E. (1983). On equatorial waves and El Niño. I. Influence of initial states on wave-induced currents and warming. *Journal of Physical Oceanography*, 13, 936–948. [http://doi.org/10.1175/1520-0485\(1983\)013<0936:OEWAEN>2.0.CO;2](http://doi.org/10.1175/1520-0485(1983)013<0936:OEWAEN>2.0.CO;2)
- Seiki, A., & Takayabu, Y. N. (2007). Westerly wind bursts and their relationship with intraseasonal variations and ENSO. Part II: Energetics over the Western and Central Pacific. *Monthly Weather Review*, 135(10), 3346–3361. <https://doi.org/10.1175/MWR3503.1>
- Seo, K.-H. H., & Xue, Y. (2005). MJO-related oceanic Kelvin waves and the ENSO cycle: A study with the NCEP Global Ocean Data Assimilation System. *Geophysical Research Letters*, 32, L07712. <http://doi.org/10.1029/2005GL022511>
- Shinoda, T., Kiladis, G. N., & Roundy, P. E. (2009). Statistical representation of equatorial waves and tropical instability waves in the Pacific Ocean. *Atmospheric Research*, 94(1), 37–44. <https://doi.org/10.1016/j.atmosres.2008.06.002>
- Shinoda, T., Roundy, P. E., & Kiladis, G. N. (2008). Variability of intraseasonal Kelvin waves in the equatorial Pacific Ocean. *Journal of Physical Oceanography*, 38(5), 921–944. <https://doi.org/10.1175/2007JPO3815.1>
- Slingo, J. M., Rowell, D. P., Sperber, K. R., & Nortley, F. (1999). On the predictability of the interannual behavior of the Madden-Julian oscillation and its relationship with El Niño. *Quarterly Journal of the Royal Meteorological Society*, 125(554), 583–610. <http://doi.org/10.1002/qj.4971255411>
- Stevenson, J. W., & Niiler, P. P. (2002). Upper ocean heat budget during the Hawaii-to-Tahiti shuttle experiment. *Journal of Physical Oceanography*, 13(10), 1894–1907. [http://doi.org/10.1175/1520-0485\(1983\)013<1894:uohbdt>2.0.co;2](http://doi.org/10.1175/1520-0485(1983)013<1894:uohbdt>2.0.co;2)
- Thomson, R. E., & Davis, E. E. (2017). Equatorial Kelvin waves generated in the western tropical Pacific Ocean trigger mass and heat transport within the Middle America Trench off Costa Rica. *Journal of Geophysical Research: Oceans*, 122, 5850–5869. <https://doi.org/10.1002/2017JC012848>
- Thomson, W. (1880). On gravitational oscillation of rotating water. *Proceedings of the Royal Society of Edinburgh*, 10, 92–100. <http://doi.org/10.1017/S0370164600043467>
- Townsend, T. L., Barron, C. N., & Helber, R. W. (2015). Ocean prediction with Improved Synthetic Ocean Profiles (ISOP). Retrieved from <https://www7320.nrlssc.navy.mil/pubs/2015/townsend-2015.pdf>
- Vecchi, G. A., & Harrison, D. E. (2000). Tropical Pacific sea surface temperature anomalies, El Niño, and equatorial westerly wind events. *Journal of Climate*, 13(11), 1814–1830. [https://doi.org/10.1175/1520-0442\(2000\)013<1814:TPSSTA>2.0.CO;2](https://doi.org/10.1175/1520-0442(2000)013<1814:TPSSTA>2.0.CO;2)
- Ventrice, M. J., Wheeler, M. C., Hendon, H. H., Schreck, C. J., Thorncroft, C. D., & Kiladis, G. N. (2013). A modified multivariate Madden-Julian Oscillation index using velocity potential. *Monthly Weather Review*, 141(12), 4197–4210. <https://doi.org/10.1175/MWR-D-12-00327.1>
- Wang, S., Ma, D., Sobel, A. H., & Tippet, M. K. (2018). Propagation characteristics of BSISO indices. *Geophysical Research Letters*, 45, 9934–9943. <http://doi.org/10.1029/2018GL078321>
- Wheeler, M. C., & Hendon, H. H. (2004). An all-season real-time multivariate MJO Index: Development of an index for monitoring and prediction. *Monthly Weather Review*, 132(8), 1917–1932. [https://doi.org/10.1175/1520-0493\(2004\)132<1917:AARMMI>2.0.CO;2](https://doi.org/10.1175/1520-0493(2004)132<1917:AARMMI>2.0.CO;2)

- Woolnough, S. J., Slingo, J. M., & Hoskins, B. J. (2000). The relationship between convection and sea surface temperature on intraseasonal timescales. *Journal of Climate*, *13*(12), 2086–2104. [https://doi.org/10.1175/1520-0442\(2000\)013<2086:TRBCAS>2.0.CO;2](https://doi.org/10.1175/1520-0442(2000)013<2086:TRBCAS>2.0.CO;2)
- Wyrtki, K. (1975). El Niño—The dynamic response of the equatorial Pacific Ocean to atmospheric forcing. *Journal of Physical Oceanography*, *5*(4), 572–584. [http://doi.org/10.1175/1520-0485\(1975\)005<0572:ENTDRO>2.0.CO;2](http://doi.org/10.1175/1520-0485(1975)005<0572:ENTDRO>2.0.CO;2)
- Wyrtki, K. (1977). Sea level during the 1972 El Niño. *Journal of Physical Oceanography*, *7*(6), 779–787. [https://doi.org/10.1175/1520-0485\(1977\)007<0779:SLDTEN>2.0.CO;2](https://doi.org/10.1175/1520-0485(1977)007<0779:SLDTEN>2.0.CO;2)
- Yu, Z., Metzger, E. J., & Fan, Y. (2017). The impact of ocean surface currents on Sverdrup transport in the midlatitude North Pacific via the wind stress formulation. *Journal of Physical Oceanography*, *47*(3), 603–614. <https://doi.org/10.1175/JPO-D-16-0155.1>
- Yu, Z., Metzger, E. J., Thoppil, P., Hurlburt, H. E., Zamudio, L., Smedstad, O. M., et al. (2015). Seasonal cycle of volume transport through Kerama Gap revealed by a 20-year global HYbrid Coordinate Ocean Model reanalysis. *Ocean Modelling*, *96*, 203–213. <https://doi.org/10.1016/j.ocemod.2015.10.012>
- Zhang, C. (2001). Intraseasonal perturbations in sea surface temperatures of the equatorial eastern Pacific and their association with the Madden-Julian Oscillation. *Journal of Climate*, *14*(6), 1309–1322. [https://doi.org/10.1175/1520-0442\(2001\)014<1309:IPISST>2.0.CO;2](https://doi.org/10.1175/1520-0442(2001)014<1309:IPISST>2.0.CO;2)
- Zhang, C., & Gottschalck, J. (2002). SST anomalies of ENSO and the Madden-Julian oscillation in the equatorial Pacific. *Journal of Climate*, *15*(17), 2429–2445. [https://doi.org/10.1175/1520-0442\(2002\)015<2429:SAOEAT>2.0.CO;2](https://doi.org/10.1175/1520-0442(2002)015<2429:SAOEAT>2.0.CO;2)